Low-overhead Parametric Estimation and Pilot-Data Resource Trade-off in an RIS-Aided Near-field Communication System

Shivani Dhok, *Student Member, IEEE*, and Neelesh B. Mehta, *Fellow, IEEE*

***Abstract*—In the near-field of a reconfigurable intelligent surface (RIS), the steering vector of the channel between the RIS and a user depends on both azimuth and distance. As a result, new channel estimation schemes, which are required for configuring the RIS and data demodulation, are needed. We study a low-training-overhead parametric maximum-likelihood (ML) scheme that estimates the directional cosine, distance, and complex gain to reconstruct the RIS-to-user channel gain. We derive novel expressions for the Cramér-Rao lower bound for the mean square error (MSE) of the estimated channel parameters and the RIS-to-user channel gain. Using the asymptotic efficiency of the ML estimate, we present novel, insightful expressions for the statistics of the cascaded channel gain between the access point and the user in the presence of errors in configuring the RIS. These are also essential for building its linear minimum MSE estimator. We then derive an expression for the achievable rate in the presence of estimation errors, which leads to insightful, closed-form expressions for the optimal pilot and data powers. Our approach requires fewer pilots than the number of RIS elements and achieves a lower MSE and a higher rate than several benchmarking schemes.**

***Index Terms*—Near-field communication, Reconfigurable intelligent surfaces, Channel estimation, Achievable rate, Cramér-Rao lower bound, Parametric maximum-likelihood estimation.**

I. Introduction

Sixth-generation (6G) wireless communication systems are expected to support new data-hungry applications such as digital replicas, augmented reality, virtual reality, extended reality, and holographic videos [2]. To do so, higher carrier frequencies, where considerable bandwidth is available, are being considered. Furthermore, techniques such as extremely large multi-input multi-output (MIMO) and extremely large aperture arrays are being actively investigated [2]. The move to larger aperture arrays, more antennas, and higher carrier frequencies makes the user fall in the near-field of the transmitter [3]. This is because the Fraunhofer distance, which demarcates the far-field and near-field regions, increases as the product of the square of the array aperture and the carrier frequency. Hence, near-field is emerging as an important regime of communication [4].

S. Dhok and N. B. Mehta are with the Dept. of Electrical Communication Eng. at the Indian Institute of Science (IISc), Bangalore, India. Emails: shivanid17499@gmail.com, nbmehta@iisc.ac.in

The work of S. Dhok was supported by the Prime Minister's Research Fellowship (PMRF). The work of N. B. Mehta was supported by the J. C. Bose Fellowship JCB/2023/000028.

Preliminary results related to this work have been accepted for presentation in IEEE GLOBECOM 2025, Taipei, Taiwan [1].

Wavefronts that are planar in the far-field region become spherical in the near-field region. As a result, the steering vector of the near-field channel depends not only on the angle-of-arrival/departure (AoA/AoD) between the transmitter and the receiver, as is the case in the far-field, but also on the distance. This distance dependency in the near-field enables sharp *beamfocusing* [3] and joint localization and channel estimation [5]. It allows the transmitter to communicate with two users along the same angular direction [3]. This fundamental change in the channel model makes conventional far-field-based techniques inapplicable or sub-optimal in the near-field.

Another 6G technology where near-field applies is a large reconfigurable intelligent surface (RIS). An RIS is an array of near-passive elements made from metamaterials. It can focus or nullify the signal energy at the desired location by controlling the reflection coefficients of its elements [6], [7]. To control the phases of its elements, the knowledge of the cascaded channels between the transmitter, the RIS elements, and the receiver is essential, and is acquired using channel estimation schemes.

The channel estimation schemes when the user falls in the near-field of an RIS can be broadly classified as parametric [6], compressed sensing-based [5], [8]–[10], and codebook-based schemes [11]. These vary from the far-field schemes, for which we refer the reader to [12], [13] and the references therein.

a) Parametric Schemes: In these schemes, the parameters that define the channel are estimated using non-Bayesian approaches, such as best linear unbiased and maximum-likelihood (ML) estimators, where the probability distribution of the parameters to be estimated is not required [14]. These schemes are appealing because, in principle, the number of pilots required is of the order of the number of parameters to be estimated. Such schemes have also been used for MIMO and orthogonal frequency division multiplexing systems; see [15], [16] and the references therein. More recently, these have been explored for near-field RIS [6].

b) Compressed Sensing-based Schemes: These schemes exploit the sparsity of the near-field channel. They are philosophically similar to the parametric schemes in that they reconstruct a higher-dimensional channel by estimating a few parameters using fewer pilots. In [8], a wideband spherical-domain dictionary that accounts for the beam-squint effect in the near-field is designed. A low-complexity, three-dimensional, compressed sensing-based channel estimation scheme for an extremely large RIS and a hybrid millimeter wave beamfocusing architecture at the access point (AP) is

presented in [9]. In [10], a frequency-dependent, RIS-assisted channel estimation scheme is presented that uses the polar-domain sparsity of the steering vector. In [5], a downsampled covariance matrix is constructed by eliminating the distance-dependent entries of the channel covariance matrix. This matrix is used to estimate the AoAs using the method of projections. The distances and the complex gains are then estimated using grid-search and orthogonal matching pursuit (OMP), respectively. Similar approaches have also been explored for near-field MIMO [17], [18].

c) Codebook-based Schemes: A two-step hierarchical channel estimation scheme is proposed in [11]. First, the dominant angular direction is estimated using the discrete Fourier transform (DFT) codebook. Then, the near-field codebook of [17] with codewords corresponding to angles in the neighborhood of the estimated dominant angular direction is used to estimate the exact distance and angle bins.

The noises in the channel estimation process affect the RIS-aided system in multiple ways. First, the RIS configuration is affected because the estimated channel gain is used to set it. An improper RIS configuration leads to beamfocusing misalignment and imperfect spatial focusing. Second, after the RIS is configured, the estimate of the gain of the cascaded AP-RIS-user channel, which is required for coherent data demodulation, is also affected by noise. The net effect of the noises and the pilot transmission overhead is a reduction in the achievable rate. While increasing the number of pilots and the pilot powers improves the channel estimation accuracy, it also reduces the time and power available for data transmission. The system is also affected by hardware imperfections [19] and phase noise.

A. Contributions

We study an alternate, low-overhead parametric channel estimation scheme when the user lies in the near-field of the RIS. We also characterize the fundamental trade-off between the number of pilots and their powers, and the number of data symbols and their powers, and optimize the achievable rate of this scheme. While such a trade-off has been studied for the far-field [12], [13], to the best of our knowledge, ours is the first work that analyzes it for the near-field. Moreover, the sensitivity of the estimation errors of such a parametric scheme to noise, pilot power, and number of pilots and the non-linear dependence of the near-field channel gain on the estimated parameters requires us to develop new analytical tools. The following are our contributions:

1) Channel Estimation and Error Statistics: We study a two-step parametric estimation scheme. In the first step, the AP obtains ML estimates of the RIS-to-user channel parameters, namely directional cosine, distance, and complex gain, and configures the RIS. We derive a novel Cramér-Rao lower bound (CRLB) for the mean square error (MSE) of the estimated parameters and the RIS-to-user channel gain.

In the second step, the user uses a linear minimum MSE (LMMSE) estimator to estimate the AP-RIS-user cascaded channel gain. This is essential for the user to coherently demodulate the data transmitted by the AP. The novelty of this estimator is that it accounts for the impact of the noise that affected the RIS phase configuration as well as the noise during the cascaded channel gain estimation. The estimator is built on closed-form expressions for the mean and variance of the cascaded channel gain in the presence of the above estimation errors. We derive these expressions based on a novel approximation of the cascaded channel gain, which addresses the non-linear dependence of the near-field steering vector on the directional cosine, distance, complex gain, and their estimation errors.

2) Achievable Rate: We present a novel expression for achievable rate that brings out the impact of the uplink and downlink pilot powers and the number of pilots. We also show that at a high pilot signal-to-noise ratio (SNR), maximizing the rate is equivalent to maximizing a deterministic, tractable effective signal-to-interference-plus-noise ratio (SINR).

3) Optimal Power Allocation: We derive in closed-form the optimal allocation of powers to the uplink pilot, downlink pilot, and downlink data symbols that maximizes the deterministic effective SINR and, thus, the rate.

4) Numerical Results: We find that the proposed scheme requires far fewer pilots than the number of RIS elements and achieves a higher rate and lower MSE than the far-field [7], near-field codebook-based [17], compressed sensing-based [17], [20], and non-parametric schemes [14] over a wide range of various system parameters. An important insight that we glean is that much higher power should be allocated to the downlink pilot than to a data symbol.

While [6] also considered parametric estimation, it only derived an expression for the estimates and numerically plotted the MSE. On the other hand, we analytically characterize the impact of estimation errors on the cascaded channel gain, derive the expressions for the CRLB for the MSE of the parametric estimates, and extend it to the CRLB of the RIS-to-user channel gain. Furthermore, we derive the achievable rate and the optimal pilot and data powers and durations.

B. Organization and Notations

Section II presents the system model. In Section III, we derive the expressions for the estimators and the error statistics. Section IV derives the achievable rate expression and the optimal power allocation. Section V presents numerical results. Our conclusions follow in Section VI.

Notations: Matrices and vectors are written in uppercase and lowercase boldface letters, respectively. The symbols $|\cdot|$, $(\cdot)^*$, $(\cdot)^H$, $(\cdot)^T$, $\angle(\cdot)$, $\Im\{\cdot\}$, and $\Re\{\cdot\}$ denote the absolute value, complex conjugate, Hermitian transpose, transpose, angle, imaginary part, and real part, respectively. For a vector $\mathbf{x}$, $||\mathbf{x}||_p$ denotes its ℓ_p norm and $\mathbf{x}[n]$ is its n^{th} element. The notation $\mathbf{A} \succeq \mathbf{B}$ implies that $\mathbf{A} - \mathbf{B}$ is positive semi-definite. $\mathbf{x} \sim \mathcal{CN}(\boldsymbol{\mu}, \mathbf{C})$ implies that $\mathbf{x}$ is a complex Gaussian random vector with mean $\boldsymbol{\mu}$ and covariance matrix $\mathbf{C}$. The expectation with respect to the random variable X is denoted by $\mathbb{E}_X[\cdot]$ and the expectation conditioned on the random variable Y is denoted by $\mathbb{E}_X[\cdot|Y]$; the subscript is dropped when X is obvious from the context. Variance is denoted by $\text{Var}(\cdot)$. Furthermore, $o(\cdot)$ and $\mathcal{O}(\cdot)$ denote Landau's little-o and big-O notations, respectively.

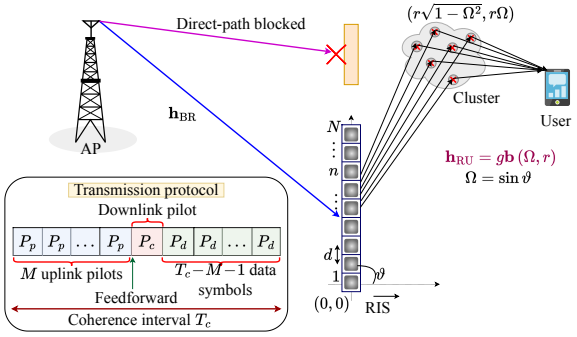

Fig. 1. System model of an RIS-assisted near-field communication system, where an AP communicates with a user with the help of an N-element RIS. Also shown is the three-step transmission protocol consisting of M uplink pilots, a downlink pilot, and $T_c - M - 1$ data symbols.

II. System Model and Transmission Protocol

As shown in Fig. 1, an AP communicates with a user with the aid of an RIS with N elements. The RIS is a uniform linear array (ULA) with an inter-element spacing of d [7], [21]. Let $\boldsymbol{\phi} \in \mathbb{C}^{N\times 1}$ be the RIS phase configuration vector, where $\boldsymbol{\phi}[n] = e^{j\theta_n}$ is the reflection coefficient of its n^{th} element with phase θ_n.

The channel between the AP and the RIS is a deterministic line-of-sight (LoS) channel with gain $\mathbf{h}_{\text{BR}} \in \mathbb{C}^{N\times 1}$, which is known perfectly to the AP and the user. This is justified when the AP-to-RIS channel gain remains constant over multiple coherence intervals of the RIS-to-user channel gain [6], [7], [22]. For example, when the AP and the RIS are fixed on towers and rooftops, the AP-to-RIS channel's AoD and distance can be estimated over multiple coherence intervals with the help of a co-located anchor node [23]. In an unmanned aerial vehicle (UAV)-assisted RIS setup, where the RIS is mounted on a UAV, the use of a co-located anchor node is not possible. However, the use of a few passive sensors at the RIS can facilitate the estimation of $\mathbf{h}_{\text{BR}}$ [24].

As illustrated in Fig. 1, we consider a single-tap, cluster-based channel model for the RIS-to-user channel gain, where the signals scattered from the multiple scatterers in the cluster arrive at the user over multiple paths. Let $\mathbf{h}_{\text{RU}} = g\mathbf{b}(\Omega, r) \in \mathbb{C}^{N\times 1}$ be the near-field non-LoS channel gain between the RIS and the user. Here, $\mathbf{b}(\Omega, r) \in \mathbb{C}^{N\times 1}$ is the near-field steering vector and g is the multipath complex gain [4, (132)]. The superposition of the signals from the multiple paths makes g a zero-mean, circularly symmetric complex Gaussian random variable. Let its variance be σ_g^2. Furthermore, $g = \beta h_1$, where $h_1 \sim \mathcal{CN}\left(0, \alpha_{\text{ref}}\left(r_{\text{ref}}/r_1\right)^{\nu}\right)$ is the diffused scattering contributed by the scatterer cluster and $\beta = \left(r_{\text{ref}}/r\right)^{\frac{\nu}{2}} e^{-j\frac{2\pi}{\lambda}r}$ is the complex gain due to the RIS-scatterer cluster path [4, (132)]. Here, λ is the wavelength, r_1 is the distance between the scatterer cluster and the user, α_{ref} is the signal power attenuation at the reference distance r_{ref}, ν is the pathloss exponent, and r is the distance between the RIS reference element located at the origin $(0,0)$ and the center of the cluster. Therefore, $\sigma_g^2 = \alpha_{\text{ref}}\left(r_{\text{ref}}^2/r_1 r\right)^{\nu}$.

The n^{th} element of the steering vector $\mathbf{b}(\Omega, r)$ is [4]

$$\mathbf{b}(\Omega, r)[n] = N^{-\frac{1}{2}} e^{-j\frac{2\pi}{\lambda}\left(-(n-1)d\Omega + \frac{1}{2r}(n-1)^2 d^2\left(1-\Omega^2\right)\right)}, \quad (1)$$

where $\Omega = \sin\vartheta$ is the directional cosine and ϑ is the azimuth angle of the cluster center relative to $(0,0)$. We assume that the direct link between the AP and the user is blocked due to obstacles [7], [25].

A. Transmission Protocol

The transmission protocol is illustrated in Fig. 1. It consists of the following three steps:

1) RIS Configuration Estimation: The user transmits M uplink pilots, each with power P_p. When the k^{th} pilot $x_p = 1$ is transmitted, the RIS configuration is set as $\boldsymbol{\phi}_k$. For example, $\boldsymbol{\phi}_k$ can be the k^{th} column of the $N \times N$ DFT matrix [26], [27]. The received signal y_k at the AP for the k^{th} pilot is

$$y_k = \sqrt{P_p}\boldsymbol{\phi}_k^T \mathbf{H}_{\text{BR}} \mathbf{h}_{\text{RU}} x_p + n_k, \quad (2)$$

where $n_k \sim \mathcal{CN}\left(0, \sigma_{\text{AP}}^2\right)$ is additive white Gaussian noise (AWGN) and $\mathbf{H}_{\text{BR}}$ is a diagonal matrix with diagonal entries as $\mathbf{h}_{\text{BR}}$. Stacking the received signals for all M pilots, we get

$$\mathbf{y} = \sqrt{P_p}\mathbf{F}_m \mathbf{H}_{\text{BR}} \mathbf{h}_{\text{RU}} + \mathbf{n} = \sqrt{P_p}\mathbf{F}_m \mathbf{H}_{\text{BR}} g\mathbf{b}(\Omega, r) + \mathbf{n}, \quad (3)$$

where $\mathbf{y} \triangleq [y_1, y_2, \ldots, y_M]^T$, $\mathbf{F}_m \triangleq [\boldsymbol{\phi}_1, \boldsymbol{\phi}_2, \ldots, \boldsymbol{\phi}_M]^T$, and $\mathbf{n} \triangleq [n_1, n_2, \ldots, n_M]^T$.

Let $\widehat{g}$, $\widehat{\Omega}$, and $\widehat{r}$ be the estimates of the parameters g, Ω, and r, respectively, that the AP obtains from $\mathbf{y}$. Then, the estimate $\widehat{\mathbf{h}}_{\text{RU}}$ of $\mathbf{h}_{\text{RU}}$ is $\widehat{\mathbf{h}}_{\text{RU}} = \widehat{g}\mathbf{b}\left(\widehat{\Omega}, \widehat{r}\right)$. Based on $\widehat{\mathbf{h}}_{\text{RU}}$, the AP sets the phase $\widehat{\boldsymbol{\phi}}[n]$ of the n^{th} RIS element as [28]

$$\widehat{\boldsymbol{\phi}}[n] = e^{-j\left(\angle \mathbf{h}_{\text{BR}}[n] + \angle \widehat{\mathbf{h}}_{\text{RU}}[n]\right)} = \frac{\mathbf{h}_{\text{BR}}^*[n]\,\widehat{\mathbf{h}}_{\text{RU}}^*[n]}{|\mathbf{h}_{\text{BR}}[n]|\left|\widehat{\mathbf{h}}_{\text{RU}}[n]\right|}. \quad (4)$$

Note that $\widehat{\boldsymbol{\phi}}[n]$ is affected by the noisy channel estimate $\widehat{\mathbf{h}}_{\text{RU}}$ in both its numerator and denominator. Thus, it is a non-linear function of $\widehat{\mathbf{h}}_{\text{RU}}$ and its estimation error.

The AP forwards the estimates $\widehat{\Omega}$ and $\widehat{r}$ to the user.

2) Cascaded Channel Gain Estimation: After setting the RIS phase configuration as per (4), the cascaded channel gain $h_{\text{eq}}\left(\widehat{\boldsymbol{\phi}}, \Omega, r\right)$ between the AP and the user, assuming channel reciprocity [6], [12], is given by $h_{\text{eq}}\left(\widehat{\boldsymbol{\phi}}, \Omega, r\right) \triangleq \sum_{n=1}^{N} \mathbf{h}_{\text{BR}}[n]\,\mathbf{h}_{\text{RU}}[n]\,\widehat{\boldsymbol{\phi}}[n]$. Substituting (4) in this, we get

$$h_{\text{eq}}\left(\widehat{\boldsymbol{\phi}}, \Omega, r\right) = \sum_{n=1}^{N} |\mathbf{h}_{\text{BR}}[n]|\,\mathbf{h}_{\text{RU}}[n]\,\frac{\widehat{\mathbf{h}}_{\text{RU}}^*[n]}{\left|\widehat{\mathbf{h}}_{\text{RU}}[n]\right|}. \quad (5)$$

Note that $h_{\text{eq}}\left(\widehat{\boldsymbol{\phi}}, \Omega, r\right)$ depends on the estimate $\widehat{\mathbf{h}}_{\text{RU}}$. It is also a non-linear function of $\widehat{g}$, $\widehat{\Omega}$, $\widehat{r}$, and their estimation errors.

To coherently demodulate data, the user needs to know $h_{\text{eq}}\left(\widehat{\boldsymbol{\phi}}, \Omega, r\right)$. For this purpose, the AP transmits a downlink pilot $x_c = 1$ with power P_c.[1] The received signal y_c at the user is

$$y_c = \sqrt{P_c} h_{\text{eq}}\left(\widehat{\boldsymbol{\phi}}, \Omega, r\right) + n_u, \quad (6)$$

[1]An alternate option for the AP is to send multiple pilots. However, this reduces the fraction of the time available for data transmission. Given that this lowers the prelog factor in the achievable rate expression, it is suboptimal [12].

where $n_u \sim \mathcal{CN}\left(0, \sigma_u^2\right)$ is AWGN. In practice, the user uses $\widehat{h}_{\text{eq}}\left(\widehat{\boldsymbol{\phi}}; \widehat{\Omega}, \widehat{r}\right)$ as it receives only $\widehat{\Omega}$ and $\widehat{r}$ from the AP. Note that the estimate depends on the noises in both channel estimation steps.

3) Downlink Data Transmission: The AP transmits $T_c - M - 1$ data symbols in the remaining time in a coherence interval of duration T_c symbols. When the AP transmits a data symbol x_d with power P_d, the user receives y_d given by

$$y_d = h_{\text{eq}}\left(\widehat{\boldsymbol{\phi}}, \Omega, r\right) x_d + n_d, \tag{7}$$

where $n_d \sim \mathcal{CN}\left(0, \sigma_u^2\right)$ is AWGN.

III. Parametric Channel Estimation

We now derive an estimate of the RIS-to-user channel gain by estimating its parameters. We then derive the LMMSE estimate of the cascaded channel gain.

A. Step 1: Estimation of RIS-to-user Channel

We do not impose any distribution on Ω and r. Therefore, we use the ML estimator. From (3), the probability density function $f(\mathbf{y}|g, \Omega, r)$ of $\mathbf{y}$ conditioned on g, Ω, and r is given by

$$f\left(\mathbf{y}|\, g, \Omega, r\right) = \left(\pi\sigma_{\text{AP}}^2\right)^{-M} e^{-\frac{\left\|\mathbf{y} - \sqrt{P_p} g \mathbf{F}_m \mathbf{H}_{\text{BR}} \mathbf{b}(\Omega, r)\right\|_2^2}{\sigma_{\text{AP}}^2}}. \tag{8}$$

The ML estimates $\widehat{g}$, $\widehat{\Omega}$, and $\widehat{r}$ can be shown to be

$$\left(\widehat{g}, \widehat{\Omega}, \widehat{r}\right) = \underset{\substack{g \in \mathbb{C} \\ r \geq r_{\min},\ \Omega \in [-1,1]}}{\operatorname{argmax}} \left\{\ln\left(f\left(\mathbf{y}|\, g, \Omega, r\right)\right)\right\}, \tag{9}$$

where $r_{\min} \triangleq 0.62\sqrt{D^3/\lambda}$ is the boundary between the reactive and radiative near-fields [4] and $D \triangleq Nd$ is the RIS aperture.

The parametric ML estimates are given by

$$\widehat{g} = \frac{\left(\mathbf{y}^H \mathbf{F}_m \mathbf{H}_{\text{BR}} \mathbf{b}\left(\widehat{\Omega}, \widehat{r}\right)\right)^*}{\sqrt{P_p}\left\|\mathbf{F}_m \mathbf{H}_{\text{BR}} \mathbf{b}\left(\widehat{\Omega}, \widehat{r}\right)\right\|_2^2}, \tag{10}$$

$$\left(\widehat{\Omega}, \widehat{r}\right) = \underset{\substack{r \geq r_{\min}, \\ \Omega \in [-1,1]}}{\operatorname{argmax}} \left\{\frac{\left|\mathbf{y}^H \mathbf{F}_m \mathbf{H}_{\text{BR}} \mathbf{b}(\Omega, r)\right|^2}{\left\|\mathbf{F}_m \mathbf{H}_{\text{BR}} \mathbf{b}(\Omega, r)\right\|_2^2}\right\}. \tag{11}$$

The proof is similar to that in [6], [7], and is skipped.

The objective function in (11) has a large number of local maxima and minima due to the complex exponential and periodic form of the steering vector (see (1)). In the near-field literature, such problems have been solved using grid-search [6]. Here, a bi-dimensional grid of size $G_\Omega \times G_r$ is set, where G_Ω is the grid size in Ω over the interval $[-1, 1]$ and G_r is the grid size in r over the interval $[r_{\min}, r_{\max}]$. Due to the periodic nature of the complex exponential of the steering vector, we set $G_\Omega = N$, which is equal to the number of resolvable angular-domain bins for an N-element ULA [29, Ch. 7]. The values of Ω and r that yield the largest value of the objective function are chosen as $\widehat{\Omega}$ and $\widehat{r}$, respectively. In general, the number of floating point operations (FLOPS) per iteration for bi-dimensional grid-search is $\mathcal{O}\left(G_r G_\Omega (NM + M)\right)$.

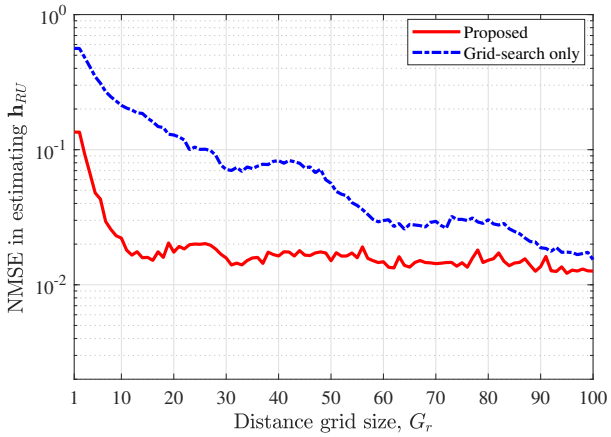

Fig. 2. NMSE in estimating the RIS-to-user channel gain as a function of G_r for our approach and the grid-search only approach ($N = 100$, $M = N/2$, $r_{\max} = 200$ m, and $\frac{MP_p\sigma_g^2|\rho_{\text{BR}}|^2}{N\sigma_{\text{AP}}^2} = 5$ dB).

We propose a lower-complexity hybrid approach that combines grid-search to find an initial point and `fmincon`, which uses gradient descent and interior-point methods to finesse it. As above, we set a bi-dimensional grid of size $G_\Omega \times G_r$ and evaluate the objective function at each grid point. The values of Ω and r that yield the largest value of the objective function are chosen as the initial condition. Then, we run gradient descent, using MATLAB's `fmincon` function, with the acquired initial condition to obtain $\widehat{\Omega}$ and $\widehat{r}$.

As above, we also set $G_\Omega = N$. To understand how to choose G_r, in Fig. 2, we plot the MSE $\mathbb{E}\left[\left\|\mathbf{h}_{\text{RU}} - \widehat{\mathbf{h}}_{\text{RU}}\right\|_2^2\right]$ in estimating $\mathbf{h}_{\text{RU}}$ as a function of G_r for our approach and the grid-search only approach. The MSE is normalized by $\mathbb{E}\left[\|\mathbf{h}_{\text{RU}}\|_2^2\right]$. The normalized MSE (NMSE) is generated using 10^4 Monte Carlo realizations of g, r, and noise, with r uniformly distributed over 5 m to 50 m. The NMSE of our approach rapidly decreases and reaches a floor for $G_r = 7 \ll N$. The NMSE of the grid-search only approach is higher and becomes closer to that of our approach when G_r is close to N. Our approach, thus, requires a coarser grid and markedly reduces the number of FLOPS. For $N = 100$, 180, 340, and 480, the computational complexity of the grid-search only approach, where $G_\Omega = G_r = N$, is $8.4\times$, $22.7\times$, $52.0\times$, and $79.7\times$, respectively, more than the proposed approach.[2]

Finally, using $\widehat{g}$, $\widehat{\Omega}$, and $\widehat{r}$, the estimate $\widehat{\mathbf{h}}_{\text{RU}}$ is

$$\widehat{\mathbf{h}}_{\text{RU}} = \widehat{g}\mathbf{b}\left(\widehat{\Omega}, \widehat{r}\right). \tag{12}$$

We summarize our proposed approach to estimate $\mathbf{h}_{\text{RU}}$ in Fig. 3. Using $\widehat{\mathbf{h}}_{\text{RU}}$, the RIS phase configuration is set as per (4).

Let $\mathbf{e}_l = [e_g, e_\Omega, e_r]^T$, where $e_g = g - \widehat{g}$, $e_\Omega = \Omega - \widehat{\Omega}$, and $e_r = r - \widehat{r}$ are the estimation errors, and $\mathbf{C}\left(g, \Omega, r\right) = \mathbb{E}\left[\mathbf{e}_l \mathbf{e}_l^H\right]$.

[2]The simulations are run using MATLAB software on a system with 128 GB RAM, Intel i9-13900 processor, and a clock speed of 3 GHz.

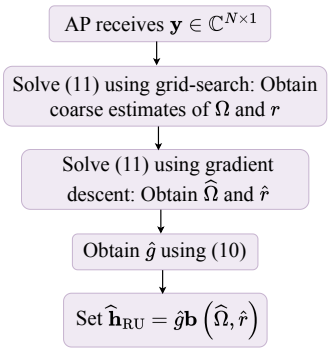

Fig. 3. Flowchart of the proposed parametric near-field ML channel estimation scheme.

B. Step 2: Cascaded channel gain Estimation

We now derive the LMMSE estimate $\widehat{h}_{\text{eq}}\left(\widehat{\boldsymbol{\phi}}; \Omega, r\right)$ of $h_{\text{eq}}\left(\widehat{\boldsymbol{\phi}}, \Omega, r\right)$. We use the LMMSE estimator to utilize the available estimates $\widehat{\Omega}$ and $\widehat{r}$ and the statistics of g. To make the derivation tractable, we initially assume that the values of the large-scale parameters Ω and r are known. Since the user knows only $\widehat{\Omega}$ and $\widehat{r}$, it uses $\widehat{h}_{\text{eq}}\left(\widehat{\boldsymbol{\phi}}; \widehat{\Omega}, \widehat{r}\right)$ as its estimator in practice. The LMMSE estimate $\widehat{h}_{\text{eq}}\left(\widehat{\boldsymbol{\phi}}; \Omega, r\right)$ is [14, (12.6)]

$$\widehat{h}_{\text{eq}}\left(\widehat{\boldsymbol{\phi}}; \Omega, r\right) = \mu_{\text{eq}} + \frac{\sqrt{P_c}\sigma_{\text{eq}}^2}{P_c\sigma_{\text{eq}}^2 + \sigma_u^2}\left(y_c - \sqrt{P_c}\mu_{\text{eq}}\right), \quad (13)$$

where μ_{eq} and σ_{eq}^2 are the mean and variance, respectively, of $h_{\text{eq}}\left(\widehat{\boldsymbol{\phi}}, \Omega, r\right)$ when Ω and r are known.

In (13), we require μ_{eq} and σ_{eq}^2. Since $h_{\text{eq}}\left(\widehat{\boldsymbol{\phi}}, \Omega, r\right)$ is a non-linear function of g, Ω, r, and their estimation errors, obtaining exact expressions for μ_{eq} and σ_{eq}^2 is difficult. We present a novel approximation for $h_{\text{eq}}\left(\widehat{\boldsymbol{\phi}}, \Omega, r\right)$ to make the problem tractable. It is motivated by our analysis of (5) in the asymptotic regime of large P_p/σ_{AP}^2 and M. While the estimator in (13) is conventional, our expressions for μ_{eq} and σ_{eq}^2 are novel and are essential for LMMSE estimation. We shall see in Section V that the approximation is accurate even for smaller values of the SNR and M.

We first derive the CRLB $\mathbf{C}_{\text{CRLB}}(g, \Omega, r)$ for estimating g, Ω, and r. It is useful for two reasons. First, it lower bounds the error covariance of any estimator, i.e., $\mathbf{C}(g, \Omega, r) \succeq \mathbf{C}_{\text{CRLB}}(g, \Omega, r)$. Second, it is tight in the asymptotic regime of a large number of pilots. This facilitates the derivation of μ_{eq} and σ_{eq}^2. Our numerical results show that the results apply even for a smaller number of pilots and at low SNRs.

To derive CRLB, we first define the following terms:

$$\begin{aligned}\boldsymbol{\partial}_g &= \frac{1}{\sqrt{P_p}}\frac{\partial}{\partial g}\left(\sqrt{P_p}\mathbf{F}_m\mathbf{H}_{\text{BR}}\mathbf{b}(\Omega, r)g\right), \\ &= \mathbf{F}_m\mathbf{H}_{\text{BR}}\mathbf{b}(\Omega, r), \quad (14)\\ \boldsymbol{\partial}_\Omega &= \frac{1}{\sqrt{P_p}g}\frac{\partial}{\partial \Omega}\left(\sqrt{P_p}\mathbf{F}_m\mathbf{H}_{\text{BR}}\mathbf{b}(\Omega, r)g\right), \\ &= \mathbf{F}_m\mathbf{H}_{\text{BR}}\left(\mathbf{b}(\Omega, r) \odot \mathbf{x}_\Omega\right), \quad (15)\end{aligned}$$

$$\begin{aligned}\boldsymbol{\partial}_r &= \frac{1}{\sqrt{P_p}g}\frac{\partial}{\partial r}\left(\sqrt{P_p}\mathbf{F}_m\mathbf{H}_{\text{BR}}\mathbf{b}(\Omega, r)g\right), \\ &= \mathbf{F}_m\mathbf{H}_{\text{BR}}\left(\mathbf{b}(\Omega, r) \odot \mathbf{x}_r\right), \quad (16)\end{aligned}$$

where the n^{th} element of $\mathbf{x}_\Omega$ and $\mathbf{x}_r$ are given by $\mathbf{x}_\Omega[n] = j\frac{2\pi}{\lambda}(n-1)d + j\frac{2\pi}{r\lambda}(n-1)^2d^2\Omega$ and $\mathbf{x}_r[n] = j\frac{\pi}{\lambda}\frac{1-\Omega^2}{r^2}(n-1)^2d^2$, and $\odot$ is the element-wise product.

From (3), we see that $\boldsymbol{\partial}_g$, $\boldsymbol{\partial}_\Omega$, and $\boldsymbol{\partial}_r$ characterize the variations in the signal component of the received pilot vector $\mathbf{y}$ with respect to g, Ω, and r, respectively. The following lemma presents $\mathbf{C}_{\text{CRLB}}(g, \Omega, r)$.

Lemma 1. *The CRLB for estimating g, Ω, and r is*

$$\mathbf{C}_{CRLB}(g, \Omega, r) = \frac{\sigma_{AP}^2}{P_p}\begin{bmatrix} \beta_{gg} & \frac{g}{2|g|^2}\beta_{g\Omega} & \frac{g}{2|g|^2}\beta_{gr} \\ \frac{g^*}{2|g|^2}\beta_{g\Omega}^* & \frac{1}{4|g|^2}\beta_{\Omega\Omega} & \frac{1}{4|g|^2}\beta_{\Omega r} \\ \frac{g^*}{2|g|^2}\beta_{gr}^* & \frac{1}{4|g|^2}\beta_{\Omega r}^* & \frac{1}{4|g|^2}\beta_{rr} \end{bmatrix}^T, \quad (17)$$

where

$$\beta_{gg} = \frac{1}{\alpha}\left(\|\boldsymbol{\partial}_\Omega\|_2^2\|\boldsymbol{\partial}_r\|_2^2 - \kappa_o^2\right), \quad (18)$$

$$\beta_{g\Omega} = \frac{1}{\alpha}\left(\boldsymbol{\partial}_g^H\boldsymbol{\partial}_r\kappa_o - \boldsymbol{\partial}_g^H\boldsymbol{\partial}_\Omega\|\boldsymbol{\partial}_r\|_2^2\right), \quad (19)$$

$$\beta_{gr} = \frac{1}{\alpha}\left(\boldsymbol{\partial}_g^H\boldsymbol{\partial}_\Omega\kappa_o - \boldsymbol{\partial}_g^H\boldsymbol{\partial}_r\|\boldsymbol{\partial}_\Omega\|_2^2\right), \quad (20)$$

$$\beta_{\Omega\Omega} = \frac{1}{\alpha}\left(2\|\boldsymbol{\partial}_g\|_2^2\|\boldsymbol{\partial}_r\|_2^2 - \left|\boldsymbol{\partial}_r^H\boldsymbol{\partial}_g\right|^2\right), \quad (21)$$

$$\beta_{\Omega r} = \frac{1}{\alpha}\left(\boldsymbol{\partial}_g^H\boldsymbol{\partial}_r\boldsymbol{\partial}_\Omega^H\boldsymbol{\partial}_g - 2\|\boldsymbol{\partial}_g\|_2^2\kappa_o\right), \quad (22)$$

$$\beta_{rr} = \frac{1}{\alpha}\left(2\|\boldsymbol{\partial}_g\|_2^2\|\boldsymbol{\partial}_\Omega\|_2^2 - \left|\boldsymbol{\partial}_\Omega^H\boldsymbol{\partial}_g\right|^2\right). \quad (23)$$

Here, $\kappa_o \triangleq \Re\left\{\boldsymbol{\partial}_\Omega^H\boldsymbol{\partial}_r\right\}$ and

$$\begin{aligned}\alpha = \|\boldsymbol{\partial}_g\|_2^2\left(\|\boldsymbol{\partial}_\Omega\|_2^2\|\boldsymbol{\partial}_r\|_2^2 - \kappa_o^2\right) + \Big[\kappa_o\Re\left\{\boldsymbol{\partial}_\Omega^H\boldsymbol{\partial}_g\boldsymbol{\partial}_g^H\boldsymbol{\partial}_r\right\} \\ -\frac{1}{2}\left(\left|\boldsymbol{\partial}_g^H\boldsymbol{\partial}_r\right|^2\|\boldsymbol{\partial}_\Omega\|_2^2 + \left|\boldsymbol{\partial}_g^H\boldsymbol{\partial}_\Omega\right|^2\|\boldsymbol{\partial}_r\|_2^2\right)\Big]. \quad (24)\end{aligned}$$

Proof: The proof is given in Appendix A. ∎

Insights: The terms $\boldsymbol{\partial}_g$, $\boldsymbol{\partial}_\Omega$, and $\boldsymbol{\partial}_r$ in (17) exhibit an oscillatory behavior with respect to Ω due to the periodic nature of the complex exponential in the near-field steering vector $\mathbf{b}(\Omega, r)$. As $|\Omega|$ approaches 1, $\boldsymbol{\partial}_r$ decreases to 0 because the distance dependency of the near-field steering vector vanishes. For large r, $\boldsymbol{\partial}_g$ and $\boldsymbol{\partial}_\Omega$ saturate to a constant value, while $\boldsymbol{\partial}_r$ decreases towards 0.

It is evident from (17) that $\mathbf{C}_{\text{CRLB}}(g, \Omega, r) \propto \sigma_{\text{AP}}^2/P_p$. It depends on g, Ω, r, the RIS phase configuration matrix $\mathbf{F}_m$, and the number of pilots M, which affects the size of $\mathbf{F}_m$. Intuitively, as M increases, the CRLB decreases because more observations are available for estimating the parameters. The CRLB also depends on the AP-to-RIS channel gain $\mathbf{h}_{\text{BR}}$, and the gradients of the steering vector $\mathbf{b}(\Omega, r)$ with respect to Ω and r through $\boldsymbol{\partial}_\Omega$ and $\boldsymbol{\partial}_r$, respectively. We numerically study this dependence on the system parameters in Section V.

For ML estimation, $\mathbf{C}(g, \Omega, r) \to \mathbf{C}_{\text{CRLB}}(g, \Omega, r)$ as M increases. Furthermore, in this regime, when conditioned on g, Ω, and r, we have $\mathbf{e}_l \sim \mathcal{CN}\left(\mathbf{0}, \mathbf{C}_{\text{CRLB}}(g, \Omega, r)\right)$ [14, (7.8)].

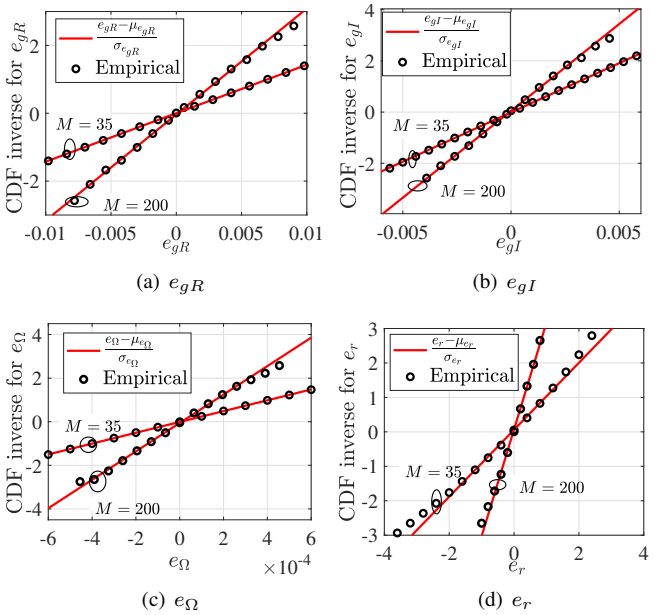

(a) e_{gR} (b) e_{gI} (c) e_Ω (d) e_r

Fig. 4. Gaussian probability paper test for e_g, e_Ω, and e_r for different values of M ($N = 100$ and $P_p |g|^2 |\rho_{\text{BR}}|^2 / (N\sigma_{\text{AP}}^2) = 3$ dB).

We now verify this. To do so, we use the Gaussian probability paper test [30, Ch. 6]. It compares $Q^{-1}(1 - F_\chi(x))$ (referred to as 'Empirical') with the line $(x - \mu_\chi)/\sigma_\chi$, where μ_χ, σ_χ^2, and $F_\chi(\cdot)$ are the empirical mean, variance, and empirical cumulative distribution function of a random variable χ. The closer the two curves are, the closer χ is to a Gaussian random variable in distribution. For the simulations, we generate 10^4 noise realizations and set $\Omega = 0.5$, $r = 20$ m, and $g = 0.1 + j0.3$.

Fig. 4(a) shows the Gaussian paper test result for $e_{gR} \triangleq \Re\{e_g\}$ for two values of M. We see that the empirical curve and $(x - \mu_{e_{gR}})/\sigma_{e_{gR}}$ become closer as M increases. Figs. 4(b), 4(c), and 4(d) show the corresponding results for $e_{gI} \triangleq \Im\{e_g\}$, e_Ω, and e_r, respectively. In all these figures, the two curves become closer to each other as M increases. We also see that the Gaussianity applies for $M = 35$, which is less than $N = 100$.

Next, we derive the CRLB $\mathbf{C}_{\text{CRLB}}(\mathbf{h}_{\text{RU}})$ for estimating the RIS-to-user channel gain $\mathbf{h}_{\text{RU}}$.

Lemma 2. *The CRLB for estimating $\mathbf{h}_{RU}$ is given by*

$$\mathbf{C}_{CRLB}(\mathbf{h}_{RU}) = \mathbf{J}_{\mathbf{h}_{RU}} \mathbf{C}_{CRLB}(g, \Omega, r) \mathbf{J}_{\mathbf{h}_{RU}}^H, \tag{25}$$

where $\mathbf{J}_{\mathbf{h}_{RU}} = [\mathbf{b}(\Omega, r),\ \mathbf{h}_{RU} \odot \mathbf{x}_\Omega,\ \mathbf{h}_{RU} \odot \mathbf{x}_r]$.

Proof: The proof is given in Appendix B. ∎

The above results lead to the following novel approximation of the cascaded channel gain $h_{\text{eq}}\left(\widehat{\boldsymbol{\phi}}, \Omega, r\right)$ as a function of the errors in estimating the parameters.

Theorem 1. *$h_{eq}\left(\widehat{\boldsymbol{\phi}}, \Omega, r\right)$ can be written as*

$$h_{eq}\left(\widehat{\boldsymbol{\phi}}, \Omega, r\right) = \frac{|g|}{\sqrt{N}} \|\mathbf{h}_{BR}\|_1$$

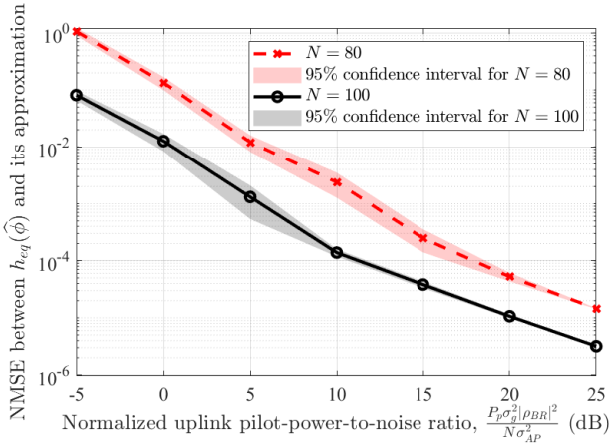

Fig. 5. NMSE between $h_{\text{eq}}\left(\widehat{\boldsymbol{\phi}}, \Omega, r\right)$ and its approximation in (26) as a function of $P_p\sigma_g^2 |\rho_{\text{BR}}|^2 / (N\sigma_{\text{AP}}^2)$ for two values of N ($M = N/2$).

$$+ \frac{|g|}{\sqrt{N}} \sum_{n=1}^{N} |\mathbf{h}_{BR}[n]| \boldsymbol{\eta}_n^T(g, \Omega, r) \mathbf{e}_l + o\left(\sqrt{\frac{\sigma_{AP}^2}{P_p}}\right), \tag{26}$$

where $\boldsymbol{\eta}_n(g, \Omega, r) \triangleq \left[g^*/\left(2|g|^2\right),\ \mathbf{x}_\Omega[n],\ \mathbf{x}_r[n]\right]^T$. *The approximation error decreases to 0 as $P_p/\sigma_{AP}^2 \to \infty$ and $M \to \infty$.*

Proof: The proof is given in Appendix C. ∎

To understand (26), consider the case when g, Ω, and r are perfectly known at the AP. In this case, $h_{\text{eq}}\left(\boldsymbol{\phi}^{\text{opt}}\right)$ is given by

$$h_{\text{eq}}\left(\boldsymbol{\phi}^{\text{opt}}\right) = \frac{|g|}{\sqrt{N}} \|\mathbf{h}_{\text{BR}}\|_1. \tag{27}$$

Therefore, the second term in (26) captures the impact of the improper RIS configuration, which is due to errors in estimating $\mathbf{h}_{\text{RU}}$, on the cascaded channel gain. This term is distance-dependent as the user is in the near-field of the RIS.

The expression in Theorem 1 is based on asymptotic expressions of P_p/σ_{AP}^2 and M. The approximation relies on the fact that $\mathbf{C}(g, \Omega, r) \to \mathbf{C}_{\text{CRLB}}(g, \Omega, r)$ for large M. It is evident from Fig. 4 and the results in Section V-A that it holds for $M \geq 35$. To understand its accuracy in the non-asymptotic regime of pilot SNR, Fig. 5 plots the MSE between $h_{\text{eq}}\left(\widehat{\boldsymbol{\phi}}, \Omega, r\right)$ and its approximation in (26), divided by the average power of $h_{\text{eq}}\left(\widehat{\boldsymbol{\phi}}, \Omega, r\right)$, as a function of $P_p\sigma_g^2 |\rho_{\text{BR}}|^2 / (N\sigma_{\text{AP}}^2)$. It does so for two values of N. The plots are generated through Monte Carlo simulations that average over 10^4 realizations of noise and g. The NMSE decreases as $P_p\sigma_g^2 |\rho_{\text{BR}}|^2 / (N\sigma_{\text{AP}}^2)$ or N increases. Furthermore, we see that the NMSE is less than 10^{-2} when $P_p\sigma_g^2 |\rho_{\text{BR}}|^2 / (N\sigma_{\text{AP}}^2)$ exceeds 7 dB and 0 dB for $N = 80$ and 100, respectively. These SNR values are reasonable in 5G systems. Also shown is the 95% confidence interval. It becomes narrower when $P_p\sigma_g^2 |\rho_{\text{BR}}|^2 / (N\sigma_{\text{AP}}^2)$ increases.

Using (26), we now present the expressions for μ_{eq} and σ_{eq}^2.

Lemma 3. *In the asymptotic regime of large M and P_p/σ_{AP}^2, the mean μ_{eq} and variance σ_{eq}^2 of $h_{eq}\left(\widehat{\boldsymbol{\phi}},\Omega,r\right)$ are given by*

$$\mu_{eq} = \sqrt{\frac{\pi\sigma_g^2}{4N}}\left\|\mathbf{h}_{BR}\right\|_1, \tag{28}$$

$$\sigma_{eq}^2 = \left(1-\frac{\pi}{4}\right)\frac{\sigma_g^2}{N}\left\|\mathbf{h}_{BR}\right\|_1^2 + \frac{\sigma_{AP}^2}{P_p N}\sum_{n=1}^{N}\sum_{m=1}^{N}\left|\mathbf{h}_{BR}[n]\right|\left|\mathbf{h}_{BR}[m]\right|\delta_{nm}, \tag{29}$$

where

$$\delta_{nm} = \frac{\beta_{gg}}{4} + \frac{\pi^2 d^2}{\lambda^2}(m-1)(n-1) \times \left(\xi_n(\Omega,r)\left[\beta_{\Omega\Omega}\xi_m(\Omega,r) + \beta_{\Omega r}^{*}\psi_m(\Omega,r)\right] + \psi_n(\Omega,r)\left[\beta_{\Omega r}\xi_m(\Omega,r) + \beta_{rr}\psi_m(\Omega,r)\right]\right), \tag{30}$$

$\xi_n(\Omega,r) = 1+\frac{\Omega d(n-1)}{r}$, *and* $\psi_n(\Omega,r) = \frac{(1-\Omega^2)(n-1)d}{2r^2}$.

Proof: The proof is given in Appendix D. ∎

Insights: When g, Ω, and r are perfectly known at the AP, we can show from (27) that $\sigma_{\text{eq}}^2 = (1-\pi/4)\,\sigma_g^2\left\|\mathbf{h}_{\text{BR}}\right\|_1^2/N$. Therefore, the second term in (29) captures the effect of the estimation errors in g, Ω, and r. It depends on P_p/σ_{AP}^2, $\mathbf{h}_{\text{BR}}$, and $\mathbf{C}_{\text{CRLB}}(g,\Omega,r)$ (through the term $\sigma_{\text{AP}}^2\delta_{nm}/P_p$).

The above result yields the following insight about the beamfocusing gain.

Corollary 1. *The beamfocusing gain G_B is given by*

$$G_B = \mathbb{E}\left[\left|h_{eq}\left(\widehat{\boldsymbol{\phi}},\Omega,r\right)\right|^2\right] = \frac{\sigma_g^2}{N}\left\|\mathbf{h}_{BR}\right\|_1^2 + \frac{\sigma_{AP}^2}{P_p N}\sum_{n=1}^{N}\sum_{m=1}^{N}\left|\mathbf{h}_{BR}[n]\right|\left|\mathbf{h}_{BR}[m]\right|\delta_{nm}. \tag{31}$$

Proof: The proof follows from (62) in Appendix D. ∎

The first term in (31) is the beamfocusing gain when g, Ω, and r are known at the AP. The second term captures the impact of the errors in estimating g, Ω, and r.

Substituting (28) and (29) in (13) yields the expression for $\widehat{h}_{\text{eq}}\left(\widehat{\boldsymbol{\phi}};\Omega,r\right)$. As mentioned, the user employs $\widehat{h}_{\text{eq}}\left(\widehat{\boldsymbol{\phi}};\widehat{\Omega},\widehat{r}\right)$ as the cascaded channel gain estimate.

C. Extensions and Open Problems

In the following, we discuss how the proposed parametric estimator can be extended to other system models.

1) *Multi-cluster Channel Model:* When the RIS-to-user channel has Q clusters, then $\mathbf{h}_{\text{RU}} = \sum_{q=1}^{Q}\mathbf{b}(\Omega_q,r_q)\,g_q$, where g_q, Ω_q, and r_q are the complex gain, directional cosine, and distance for the q^{th} cluster, respectively. Then, we can show that the estimate $\widehat{g}_q$ of g_q, for $1\le q\le Q$, is given by

$$\widehat{g}_q = \frac{\left(\mathbf{y}^H\mathbf{F}_m\mathbf{H}_{\text{BR}}\mathbf{b}\left(\widehat{\Omega}_q,\widehat{r}_q\right)\right)^*}{\sqrt{P_p}\text{tr}\left(\mathbf{A}\left(\widehat{\boldsymbol{\Omega}},\widehat{\mathbf{r}}\right)\mathbf{A}^H\left(\widehat{\boldsymbol{\Omega}},\widehat{\mathbf{r}}\right)\right)}, \tag{32}$$

where $\mathbf{A}(\boldsymbol{\Omega},\mathbf{r}) = \mathbf{F}_m\mathbf{H}_{\text{BR}}[\mathbf{b}(\Omega_1,r_1)\ldots\mathbf{b}(\Omega_Q,r_Q)]$, $\widehat{\boldsymbol{\Omega}} = \left[\widehat{\Omega}_1,\ldots,\widehat{\Omega}_Q\right]^T$, and $\widehat{\mathbf{r}} = [\widehat{r}_1,\ldots,\widehat{r}_Q]^T$. Here $\widehat{\boldsymbol{\Omega}}$ and $\widehat{\mathbf{r}}$ are the estimates of $\boldsymbol{\Omega} = [\Omega_1,\ldots,\Omega_Q]^T$ and $\mathbf{r} = [r_1,\ldots,r_Q]^T$. They are given by

$$\left(\widehat{\boldsymbol{\Omega}},\widehat{\mathbf{r}}\right) = \underset{\substack{\Omega_q\in[-1,1],\\ r_q\ge r_{\max},\\ q\in\{1,\ldots,Q\}}}{\text{argmax}}\left\{\frac{\sum_{q=1}^{Q}\left|\mathbf{y}^H\mathbf{F}_m\mathbf{H}_{\text{BR}}\mathbf{b}(\Omega_q,r_q)\right|^2}{\text{tr}\left(\mathbf{A}(\boldsymbol{\Omega},\mathbf{r})\mathbf{A}^H(\boldsymbol{\Omega},\mathbf{r})\right)}\right\}. \tag{33}$$

For $Q=1$, the above estimator reduces to that in (10) and (11). This estimator maximizes a lower bound on the log-likelihood function. The bound is based on the following inequality: $\text{tr}\left(\mathbf{A}^H(\boldsymbol{\Omega},\mathbf{r})\mathbf{A}(\boldsymbol{\Omega},\mathbf{r})\mathbf{g}\mathbf{g}^H\right) \le \text{tr}\left(\mathbf{A}^H(\boldsymbol{\Omega},\mathbf{r})\mathbf{A}(\boldsymbol{\Omega},\mathbf{r})\right)\left\|\mathbf{g}\right\|_2^2$ [31, Sec. 7.2].

2) *Uniform Planar Array (UPA) RIS:* When the elements of the RIS are arranged as a UPA, four parameters, namely azimuth AoA, elevation AoA, distance, and complex gain need to be estimated. As shown in Section V, the proposed parametric ML estimator can be easily extended to a UPA RIS.
3) *Multi-antenna AP:* For an AP with N_{AP} antennas, let $\mathbf{H}_{\text{AR}} \in \mathbb{C}^{N\times N_{\text{AP}}}$ denote the AP-to-RIS channel gain. Then, the uplink pilot vector $\mathbf{y} \in \mathbb{C}^{MN_{\text{AP}}\times 1}$ in (3) can be shown to be $\mathbf{y} = \sqrt{P_p}\mathbf{G}\mathbf{b}(\Omega,r)g + \mathbf{n}$, where $\mathbf{G} = [\text{diag}(\boldsymbol{\phi}_1)\mathbf{H}_{\text{AR}},\ldots,\text{diag}(\boldsymbol{\phi}_M)\mathbf{H}_{\text{AR}}]^T$. The parametric estimator to obtain $\widehat{g}$, $\widehat{\Omega}$, and $\widehat{r}$ can be obtained by replacing $\mathbf{F}_m\mathbf{H}_{\text{BR}}$ by $\mathbf{G}$ in (10) and (11).
4) *Multiple Users:* The users can send pilots in orthogonal time-frequency resources, as is done in far-field-based systems. The proposed estimator in (10) and (11) can be used to estimate the parameters and the channel of each user.

While our approach does extend to the above models, the following new challenges arise and lead to interesting open problems. With $Q\ge 2$ clusters, we need to invert a $3Q\times 3Q$-dimensional Fisher information matrix to obtain CRLB. Similarly, for a UPA RIS, we need to invert a 4×4 Fisher information matrix. This challenge can make the CRLB analysis and the subsequent LMMSE estimation and achievable rate analysis intractable. When the AP has multiple antennas, it needs to jointly optimize the transmit precoding vector and the RIS configuration to maximize the achievable rate at the user. However, solutions to such optimization problems are known only numerically in the literature [32]–[34]. Therefore, characterizing the impact of noisy estimates on the achievable rate becomes analytically challenging.

IV. Achievable Rate and Optimal Power Allocation

We now develop expressions for the achievable rate and optimal power allocation. In principle, these need to be obtained considering the estimation error $\widehat{h}_{\text{eq}}\left(\widehat{\boldsymbol{\phi}};\widehat{\Omega},\widehat{r}\right) - h_{\text{eq}}\left(\widehat{\boldsymbol{\phi}},\Omega,r\right)$. However, due to the underlying intractability, we first derive the rate and optimal power allocation using $\widehat{h}_{\text{eq}}\left(\widehat{\boldsymbol{\phi}};\Omega,r\right)$ and then replace Ω and r by their estimates. We assess the efficacy of this approximation in Section V-B.

Let $e_{\text{eq}} \triangleq h_{\text{eq}}\left(\widehat{\boldsymbol{\phi}}, \Omega, r\right) - \widehat{h}_{\text{eq}}\left(\widehat{\boldsymbol{\phi}}; \Omega, r\right)$ denote the error in estimating the cascaded channel gain. Then, y_d in (7) equals

$$y_d = \widehat{h}_{\text{eq}}\left(\widehat{\boldsymbol{\phi}}; \Omega, r\right) x_d + e_{\text{eq}} x_d + n_d. \tag{34}$$

The term $e_{\text{eq}} x_d + n_d$ captures the net effect of the estimation error and the noise.

Theorem 2. *The achievable rate R is given by*

$$R = \left(1 - \frac{M+1}{T_c}\right) \times \mathbb{E}\left[\log_2\left(1 + \Gamma_{\mathit{eff}}\left(P_p, P_c, P_d\right)\left|\widetilde{h}_{\mathit{eq}}\left(\widehat{\boldsymbol{\phi}}\right)\right|^2\right)\right], \tag{35}$$

where

$$\Gamma_{\mathit{eff}}\left(P_p, P_c, P_d\right) = \frac{P_d\left[\left|\mu_{\mathit{eq}}\right|^2\left(P_c\sigma_{\mathit{eq}}^2 + \sigma_u^2\right) + P_c\sigma_{\mathit{eq}}^4\right]}{\left(P_d + P_c\right)\sigma_{\mathit{eq}}^2\sigma_u^2 + \sigma_u^4}, \tag{36}$$

$$\widetilde{h}_{\mathit{eq}}\left(\widehat{\boldsymbol{\phi}}\right) = \left(\left|\mu_{\mathit{eq}}\right|^2 + \frac{P_c\sigma_{\mathit{eq}}^4}{P_c\sigma_{\mathit{eq}}^2 + \sigma_u^2}\right)^{-\frac{1}{2}} \widehat{h}_{\mathit{eq}}\left(\widehat{\boldsymbol{\phi}}; \Omega, r\right). \tag{37}$$

Proof: The proof is given in Appendix E. ∎

The prelog term $\left(1 - [M+1]/T_c\right)$ in (35) accounts for the time spent on all the pilot transmissions.[3]

A. Optimal Power Allocation

In (35), R is written in terms of a unit power random variable $\widetilde{h}_{\text{eq}}\left(\widehat{\boldsymbol{\phi}}\right)$. One subtlety, which makes it difficult to directly optimize the rate expression in (35), is that the probability distribution of $\widetilde{h}_{\text{eq}}\left(\widehat{\boldsymbol{\phi}}\right)$ still depends on P_p and P_c. However, as we show below, this dependence disappears for large $P_p\sigma_g^2/\sigma_{\text{AP}}^2$ and $P_c\sigma_g^2/\sigma_u^2$.

Corollary 2. *For large M, $P_p\sigma_g^2/\sigma_{AP}^2$, and $P_c\sigma_g^2/\sigma_u^2$, $R \to \widetilde{R}$, where*

$$\widetilde{R} \triangleq \left(1 - \frac{M+1}{T_c}\right)\mathbb{E}\left[\log_2\left(1 + \Gamma_{\mathit{eff}}\left(P_p, P_c, P_d\right)\frac{|g|^2}{\sigma_g^2}\right)\right]. \tag{38}$$

Proof: The proof is given in Appendix F. ∎

A key point to note is that in (38), $|g|^2/\sigma_g^2$ is a unit mean exponential random variable, whose distribution is not a function of P_p, P_c, and P_d. Hence, maximizing $\widetilde{R}$ is equivalent to maximizing $\Gamma_{\text{eff}}\left(P_p, P_c, P_d\right)$, which we shall refer to as the *deterministic effective SINR*. We maximize it under the following constraints:

1) *Energy Budget at the User:* The energy consumed by the user in the M uplink pilot transmissions of the RIS configuration estimation step with symbol duration T_s is MP_pT_s. It should not exceed the total energy budget E_{UE} available at the user, i.e., $MP_p \le E_{\text{UE}}/T_s$. This also implies a total power constraint on the user.
2) *Energy Budget at the AP:* The energy consumed by the AP in the downlink pilot and data transmissions is $\left(P_c + \left(T_c - M - 1\right)P_d\right)T_s$. Let E_{AP} be the available energy budget at the AP. Hence, $P_c + \left(T_c - M - 1\right)P_d \le E_{\text{AP}}/T_s$. This also implies a total power constraint on the AP.

Therefore, the optimization problem can be stated as

$$\begin{aligned}
\mathcal{Q}: \quad \max_{P_p, P_c, P_d} \quad & \left\{\Gamma_{\text{eff}}\left(P_p, P_c, P_d\right)\right\}, && \text{(39a)}\\
\text{s.t.} \quad & MP_p \le E_{\text{UE}}/T_s, && \text{(39b)}\\
& P_c + \left(T_c - M - 1\right)P_d \le E_{\text{AP}}/T_s, && \text{(39c)}\\
& P_p \ge 0, P_d \ge 0, P_c \ge 0. && \text{(39d)}
\end{aligned}$$

The optimal powers $P_p^\star$, $P_c^\star\left(\Omega, r\right)$, and $P_d^\star\left(\Omega, r\right)$, when Ω and r are known, are as follows.

Theorem 3. *The optimal power allocation that solves $\mathcal{Q}$ is*

$$P_p^\star = \frac{E_{UE}}{T_sM}, \tag{40}$$

$$P_d^\star\left(\Omega, r\right) = \varrho - \sqrt{\frac{\varrho}{T_c - M - 1}}\sqrt{\varrho + \frac{\sigma_u^2}{\left|\mu_{\mathit{eq}}\right|^2 + \sigma_{\mathit{eq}}^2}}, \tag{41}$$

$$P_c^\star\left(\Omega, r\right) = \frac{E_{AP}}{T_s} - \left(T_c - M - 1\right)P_d^\star\left(\Omega, r\right), \tag{42}$$

where $\varrho = \frac{\left(E_{AP}/T_s\right)\sigma_{\mathit{eq}}^2 + \sigma_u^2}{\sigma_{\mathit{eq}}^2\left(T_c - M - 2\right)}$.

Proof: The proof is given in Appendix G. ∎

Equation (40) implies that the M uplink pilots are allocated equal powers. The optimal values of $P_d^\star\left(\Omega, r\right)$ and $P_c^\star\left(\Omega, r\right)$ in (41) and (42) depend on E_{AP} and E_{UE}. They also depend on μ_{eq} and σ_{eq}^2, which depend on the uplink pilot power.

Since the AP knows only $\widehat{\Omega}$ and $\widehat{r}$, it uses $P_d^\star\left(\widehat{\Omega}, \widehat{r}\right)$ and $P_c^\star\left(\widehat{\Omega}, \widehat{r}\right)$ for the downlink pilot and data transmissions in practice.

V. Simulation Results

We now present Monte Carlo results to quantify the dependence of the achievable rate on the system parameters and assess the accuracy of our analytical approach. For the AP-to-RIS channel, we set $\mathbf{h}_{\text{BR}} = \sqrt{N}\rho_{\text{BR}}\mathbf{b}\left(\Omega_\phi, r_\phi\right)$. The simulation parameters are given in Table I. The Fraunhofer distance R_f turns out to be 50 m. We shall refer to $\Upsilon_{\text{AP}} \triangleq E_{\text{AP}}\sigma_g^2\left|\rho_{\text{BR}}\right|^2/\left(T_sN\sigma_u^2\right)$ and $\Upsilon_{\text{UE}} \triangleq E_{\text{UE}}\sigma_g^2\left|\rho_{\text{BR}}\right|^2/\left(T_sN\sigma_{\text{AP}}^2\right)$ as the normalized energy budget at the AP and the user, respectively. Υ_{UE} and Υ_{AP} physically correspond the uplink and downlink fading-average energy budget-to-noise-ratio per RIS element, respectively.[4] We use

[3] Eq. (35) is the achievable rate when $\mathbb{E}\left[e_{\text{eq}}|\widehat{h}_{\text{eq}}\left(\widehat{\boldsymbol{\phi}}; \Omega, r\right)\right] = 0$ [35]. Since $\widehat{h}_{\text{eq}}\left(\widehat{\boldsymbol{\phi}}; \Omega, r\right)$ is the LMMSE estimate of $h_{\text{eq}}\left(\widehat{\boldsymbol{\phi}}, \Omega, r\right)$, this condition would be satisfied when $h_{\text{eq}}\left(\widehat{\boldsymbol{\phi}}, \Omega, r\right)$ is a complex Gaussian random variable. However, from (26), $h_{\text{eq}}\left(\widehat{\boldsymbol{\phi}}, \Omega, r\right)$ is not a complex Gaussian random variable in our system model. Hence, (35) is an approximate expression for the achievable rate. The approximation, which is widely used in literature, makes the problem tractable and yields valuable insights about the impact of noisy channel estimates of $\mathbf{h}_{\text{RU}}$ and $h_{\text{eq}}\left(\widehat{\boldsymbol{\phi}}, \Omega, r\right)$ on the rate and the power allocation.

[4] In Table I, $\Upsilon_{\text{AP}} = -5$ dB implies that the AP's total power E_{AP}/T_s is 20.3 dBm, which is apportioned between the downlink pilot and data as per Theorem 3.

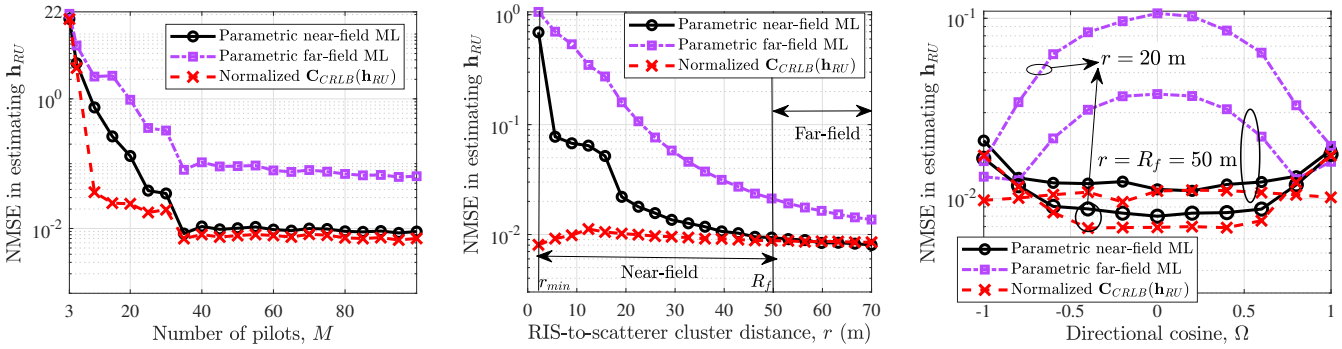

(a) As a function of M ($\Omega = 0.5$). (b) As a function of r ($M = N/2$ and $\Omega = 0.5$). (c) As a function of Ω ($M = N/2$).

Fig. 6. NMSE in estimating $\mathbf{h}_{\text{RU}}$ for the near-field and far-field models as a function of M, r, and Ω ($\Upsilon_{\text{UE}} = 5$ dB).

TABLE I
SIMULATION PARAMETERS

Parameter	*Notation*	*Value*
Pathloss exponent	ν	2.7
Reference distance	r_{ref}	1 m
Signal power attenuation at r_{ref}	α_{ref}	-20 dB
Scatterer cluster-to-user distance	r_1	10 m
RIS-to-scatterer cluster distance	r	20 m
AP-to-RIS distance	r_ϕ	10 m
RIS-to-user directional cosine	Ω	0.5
AP-to-RIS directional cosine	Ω_ϕ	0.2
Noise variance at user and AP	σ_u^2, σ_{AP}^2	-103.8 dBm
Carrier frequency	f_c	30 GHz
RIS inter-element spacing	d	$\lambda/2$
AP-to-RIS channel pathloss	$\lvert\rho_{\text{BR}}\rvert^2$	-27 dB
Normalized energy budget at AP	Υ_{AP}	-5 dB
Number of RIS elements	N	100
Distance grid size	G_r	7
Maximum distance for grid-search	$r_{\max}$	200 m

M uniformly spaced $N \times N$ DFT matrix columns in the RIS configuration estimation step. We average over 10^4 realizations of the channel and noise.

In Section V-A, we study the NMSE in estimating $\mathbf{h}_{\text{RU}}$. In Section V-B, we study its implications on the achievable rate and the optimal number of pilots and their powers.

A. NMSE

Fig. 6(a) plots the NMSE $\mathbb{E}\left[||\mathbf{h}_{\text{RU}} - \widehat{\mathbf{h}}_{\text{RU}}||_2^2\right]/\mathbb{E}\left[||\mathbf{h}_{\text{RU}}||_2^2\right]$ in estimating $\mathbf{h}_{\text{RU}}$ as a function of the number of pilots M. We compare the NMSE from parametric estimation for the near-field and far-field models. For both models, the NMSE decreases as M increases and then reaches a floor at $M = 35$. The floor occurs because $P_p^\star$ decreases as M increases (see (40)). The floor for the far-field model, which neglects the dependence of $\mathbf{h}_{\text{RU}}$ on r, is $7.14\times$ higher than that for the near-field model. An important observation is that the number of pilots required to reach the floor is more than the number of parameters to be estimated. However, it is still significantly smaller than N. The NMSE can be very large for small M. Thus, the parametric estimates are sensitive to noise for small M. Also shown is the normalized CRLB $\text{tr}\left(\mathbf{C}_{\text{CRLB}}\left(\mathbf{h}_{\text{RU}}\right)\right)/\mathbb{E}\left[\|\mathbf{h}_{\text{RU}}\|_2^2\right]$. The near-field model reaches it for $M \geq 35$.

Fig. 6(b) plots the NMSE as a function of the RIS-to-scatterer cluster distance r.[5] For $r < R_f$, the NMSE of the far-field model is significantly higher than that of the near-field model. The two NMSEs approach each other once r exceeds R_f. Also shown is the normalized CRLB. The CRLB marginally increases when r increases from $r_{\min} = 2.2$ m to 15 m. This is an artifact of our using equispaced odd-numbered columns of the DFT matrix as RIS configurations during uplink pilot transmissions. However, the CRLB decreases for $r > 15$ m. Our approach reaches the CRLB for $r > 30$ m.

Fig. 6(c) plots the NMSE as a function of Ω for different values of r. For the near-field model, the NMSE is insensitive to changes in r and Ω. However, for the far-field model, the NMSE initially increases, attains a peak at $\Omega = 0$, and then decreases. The peak occurs at $\Omega = 0$ because the second, distance-dependent term in (1) dominates the first, far-field term the most at $\Omega = 0$. By the same logic, r has a negligible impact on the near-field steering vector when $|\Omega|$ is close to 1. Hence, in this regime, the NMSEs of the near-field and the far-field models are comparable. The NMSEs of both models become closer as r increases. The NMSE of the near-field model is close to the normalized CRLB for all Ω.

B. Optimal Power Allocation and Pilots, and Benchmarking

Fig. 7 plots the ratio $P_c^\star/P_d^\star$ (in dB) of the optimal downlink pilot and data powers as a function of N for different values of Υ_{AP}. We see that $P_c^\star/P_d^\star \gg 1$. Thus, substantially more power should be allocated to the pilot symbol than a data symbol in the near-field. As N increases, $P_c^\star/P_d^\star$ decreases. This is because, as N increases, the estimation errors in each entry in $\mathbf{h}_{\text{RU}}$ accumulate and affect $h_{\text{eq}}\left(\widehat{\phi}, \Omega, r\right)$. Hence, to improve the rate, the data power $P_d^\star$ increases. As Υ_{AP} increases, $P_c^\star/P_d^\star$ decreases. This is because the smaller cascaded channel gain estimation errors enable more power to be allocated for data transmission.

[5]We shall see in Section V-B that the optimal number of pilots is in the range of $[0.3N, 0.5N]$. Hence, we set $M = N/2$ in this figure.

This article has been accepted for publication in IEEE Transactions on Communications. This is the author's version which has not been fully edited and content may change prior to final publication. Citation information: DOI 10.1109/TCOMM.2025.3644490

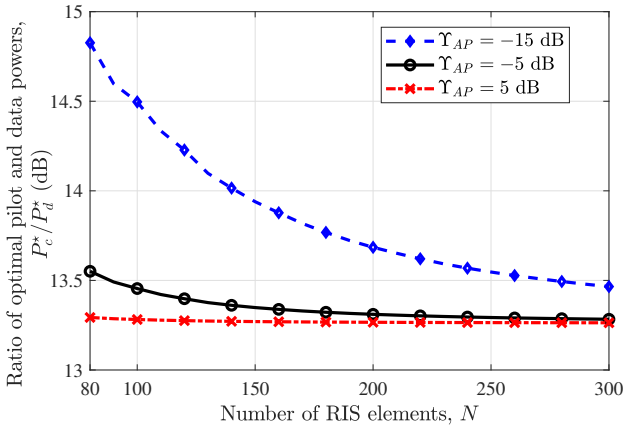

Fig. 7. Ratio of optimal downlink pilot power to data power $P_c^\star/P_d^\star$ as a function of N ($\Upsilon_{\text{UE}} = -5$ dB, $\Omega = 0.5$, and $M = 50$).

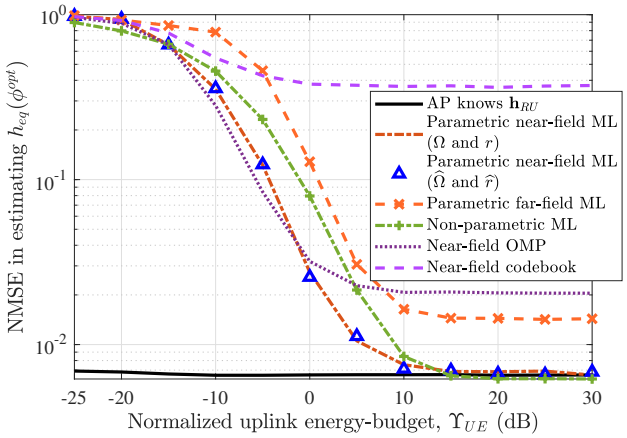

Fig. 8. NMSE in estimating $h_{\text{eq}}\left(\boldsymbol{\phi}^{\text{opt}}\right)$ as a function of Υ_{UE} for different benchmarking schemes ($\Omega = 0.5$).

Next, we benchmark our proposed scheme, which we refer to as 'Parametric near-field ML ($\widehat{\Omega}$ and $\widehat{r}$)', with the following schemes:

1) *Parametric Near-field ML (Ω and r)*: Parametric near-field estimation is used. The cascaded channel gain estimation and the optimal power allocation are done using true values of Ω and r.
2) *Parametric Near-field ML ($\widehat{\Omega}$ and $\widehat{r}$) with Equal Power Allocation (EPA):* Near-field parametric estimation is used. However, equal power is allocated to the downlink data and pilots. Thus, $P_d = P_c = E_{\text{AP}}/\left(T_s(T_c - M)\right)$.
3) *Parametric Far-field ML [7]:* The parametric channel estimation is designed assuming the far-field model. Thus, only Ω and g are estimated and the estimate $\widehat{\Omega}$ is used for cascaded channel gain estimation and power allocation.
4) *Parametric Far-field ML with EPA:* Here, the above far-field parametric channel estimation is used except that the downlink pilot and data powers are equal.
5) *Non-parametric ML:* The ML estimate $\widehat{\mathbf{h}}_{\text{RU}}$ of the RIS-to-user channel gain is given by $\widehat{\mathbf{h}}_{\text{RU}} = (\mathbf{F}_m\mathbf{H}_{\text{BR}})^\dagger\mathbf{y}/\sqrt{P_p}$, where $(\cdot)^\dagger$ is the Moore-Penrose inverse. Here, $M \geq N$.
6) *Near-field Codebook [17]:* First, $M_1 = \lceil M/2 \rceil$ pilots are sent by the user to enable the AP to estimate the codeword that is closest to $\mathbf{b}(\Omega, r)$. For the m^{th} pilot, the RIS configuration is set as $\boldsymbol{\phi}_m = \sqrt{N}\mathbf{h}_{\text{BR}}^* \odot \mathbf{v}_{\text{BR}} \odot \mathbf{c}_m^*$, where $\mathbf{v}_{\text{BR}}[n] \triangleq |\mathbf{h}_{\text{BR}}[n]|^{-1}$, $\mathbf{c}_m = \mathbf{b}(\Omega_k, r_{ks})$, and $\odot$ is the element-wise product. Here, $\Omega_k = (2k - 1 - N)\lambda/(dN)$, $r_{ks} = Z_\Delta(1 - \Omega_k^2)/s$, $\forall k \in \{0, 1, \ldots, N-1\}$ and $s \in \{0, 1, \ldots, S_{\max} - 1\}$, $Z_\Delta = 2d^2N^2/\left(\lambda(1.2)^2\right)$, and $m = S_{\max}k + s + 1$. We set the $S_{\max} = 16$, which is the value used in [17]. However, we have seen from extensive simulations that the rate is insensitive to the choice of $S_{\max}$. And, $\mathbf{W} = [\mathbf{c}_1, \mathbf{c}_2, \ldots, \mathbf{c}_{NS_{\max}}]$ is the near-field codebook matrix. Its codewords are obtained by uniformly sampling Ω over the interval $[-1, 1]$ and r^{-1} over the interval $[0, 1/r_{\min}]$. The AP selects the codeword $\mathbf{c}_{m^\star}$ with the largest received signal strength. Next, the AP sends $M_2 = M - M_1$ pilots and sets $\mathbf{b}(\Omega, r) = \mathbf{c}_{m^\star}$ for the user to obtain an LMMSE estimate $\widehat{g}$ of g. Finally, the AP sets the RIS configuration as $\widehat{\boldsymbol{\phi}} = e^{-j\angle\widehat{g}}\boldsymbol{\phi}_{m^\star}$.
7) *Near-field OMP [17], [20]:* $\mathbf{h}_{\text{RU}}$ is written as $\mathbf{h}_{\text{RU}} = \mathbf{W}\mathbf{z}$, where $\mathbf{W}$ is defined above and $\mathbf{z}$ is a one-sparse vector of the complex gain. We implement the OMP algorithm with $\sqrt{P_p}\mathbf{F}_m\mathbf{H}_{\text{BR}}\mathbf{W}$ as the sensing matrix and $\mathbf{y}$ in (3) as the measurement vector to obtain $\widehat{\mathbf{z}}$. Then, $\widehat{\mathbf{h}}_{\text{RU}} = \mathbf{W}\widehat{\mathbf{z}}$.

The pilot and data powers are set as per Theorem 3 for all schemes except EPA. For all the schemes, except the proposed scheme for which we have analytical expressions, we empirically measure μ_{eq} and σ_{eq}^2 and use them for estimating $h_{\text{eq}}\left(\widehat{\boldsymbol{\phi}}, \Omega, r\right)$ and for power allocation.

Fig. 8 plots the NMSE $\mathbb{E}\left[|h_{\text{eq}}\left(\boldsymbol{\phi}^{\text{opt}}\right) - \widehat{h}_{\text{eq}}\left(\widehat{\boldsymbol{\phi}}; \widehat{\Omega}, \widehat{r}\right)|^2\right]/\mathbb{E}\left[|h_{\text{eq}}\left(\boldsymbol{\phi}^{\text{opt}}\right)|^2\right]$ in estimating the cascaded channel gain $h_{\text{eq}}\left(\boldsymbol{\phi}^{\text{opt}}\right)$ for all the schemes. We set $M = N/2$ for all the schemes except the non-parametric ML scheme, where $M = N$. Our proposed scheme has a lower NMSE than all the schemes for $\Upsilon_{\text{UE}} \geq -2$ dB. It is indistinguishable from the near-field scheme when Ω and r are known. As Υ_{UE} increases, its NMSE decreases and equals the NMSE for the case when the AP perfectly knows $\mathbf{h}_{\text{RU}}$. Here, only the noisy channel estimate of the cascaded channel gain contributes to the NMSE, which, therefore, is a horizontal line. The NMSE for the non-parametric ML scheme also approaches the NMSE when the AP perfectly knows $\mathbf{h}_{\text{RU}}$, but only for $\Upsilon_{\text{UE}} \geq 13$ dB. For $\Upsilon_{\text{UE}} < -2$ dB, the OMP scheme has a marginally smaller NMSE than the proposed scheme, but it has a higher error floor. The codebook scheme has the highest NMSE due to its limited number of pilot transmissions.

Fig. 9 plots the achievable rate R of all the schemes as a function of M. As M increases, the achievable rate initially increases for all the schemes. This is because the errors in estimating $\widehat{g}$, $\widehat{\Omega}$, and $\widehat{r}$ decrease. The achievable rates of all the schemes decrease as M further increases because less time is available for data transmission. For the non-parametric ML scheme, we can show results only for $M \geq N$. Its achievable rate is maximum at $M = 100$ and decreases thereafter. The

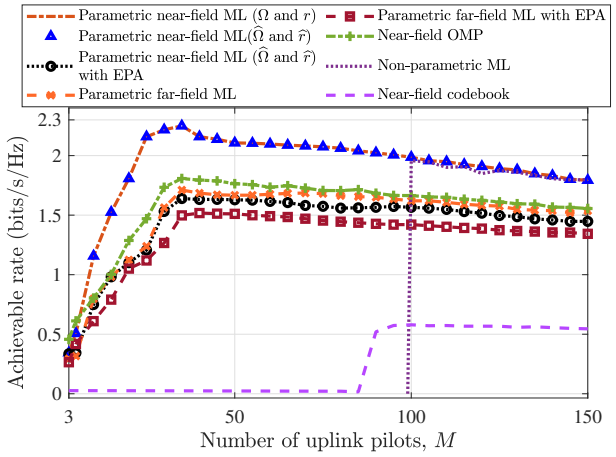

Fig. 9. Benchmarking: Achievable rate of different schemes as a function of number of pilots ($\Upsilon_{\text{UE}} = 20$ dB and $\Omega = 0$).

TABLE II
COMPARISONS OF DIFFERENT SCHEMES ($\Upsilon_{\text{UE}} = 20$ dB AND $\Omega = 0$).

Scheme	Complexity	$M^\star$	R (bits/s/Hz)
Near-field codebook	$\mathcal{O}\left(M_1 + M_2^2 + N\right)$	100	0.58
Non-parametric ML	$\mathcal{O}\left(N^2M + M\right)$	100	1.96
Near-field OMP	$\mathcal{O}\left(MNS_{\max}\right)$	35	1.81
Parametric far-field ML	$\mathcal{O}\left(N^2M + NM\right)$	35	1.71
Parametric far-field ML with EPA			1.50
Parametric near-field ML with EPA	$\mathcal{O}\left(G_r\left(N^2M + NM\right)\right)$	35	1.64
Parametric near-field ML			2.25

achievable rate of the codebook-based scheme is very low for $M < 85$ due to the coarse codebook it uses and the larger estimation errors this begets. The optimal number of pilots is 35 for the near-field parametric and far-field parametric schemes with either optimal power allocation or EPA. This is close to the value of M in Fig. 6(a) at which the MSE in estimating $\mathbf{h}_{\text{RU}}$ reaches a floor. The optimal rate of the codebook-based scheme is 3.87 times lower than that of the proposed scheme. The OMP algorithm also has a lower rate than the proposed scheme. However, it has a higher rate than all the other schemes, including near-field parametric ML with EPA.

The proposed scheme outperforms all the benchmarking schemes for all values of M. The far-field parametric ML scheme has a lower rate, even when the powers are allocated optimally. This is because it estimates only Ω but not r, which leads to a larger estimation error. Near-field and far-field EPA have lower rates due to their sub-optimal power allocations. The non-parametric ML scheme has a lower rate due to its larger training overhead. The relative performance of these benchmarking schemes is also affected by the chosen simulation parameters. We compare the complexity, optimal number of pilots, and rate of the schemes in Table II.

We now assess the optimality of the power allocation given in Theorem 3. We also assess the applicability of our insights when the RIS is a 10×10 UPA with $N = 100$ elements. For a UPA RIS, let $\widehat{g}$, $\widehat{\Omega}$, $\widehat{r}$, and $\widehat{\omega}$ denote the parametric estimates of

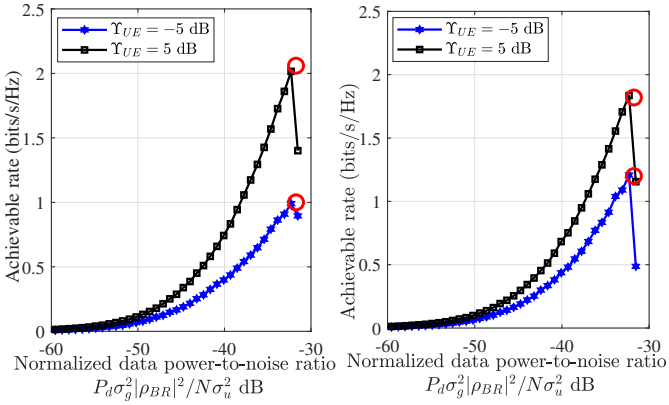

(a) ULA RIS. (b) UPA RIS.

Fig. 10. Achievable rate for ULA and UPA RIS as a function of $P_d\sigma_g^2\left|\rho_{\text{BR}}\right|^2/\left(N\sigma_u^2\right)$ ($M = N/2$ and $\Omega = 0.5$). The rate of the optimal power allocation obtained from Theorem 3 is shown as a circle ('o').

the complex gain g, the azimuth directional cosine Ω, the radial distance r, and the elevation directional cosine ω, respectively. They are given by

$$\left(\widehat{\Omega}, \widehat{\omega}, \widehat{r}\right) = \underset{\substack{\Omega,\omega\in[-1,1],\\ r\geq r_{\min}}}{\operatorname{argmax}} \left\{ \frac{\left|\mathbf{y}^H\mathbf{F}_m\mathbf{H}_{\text{BR}}\mathbf{a}_U\left(\Omega,\omega,r\right)\right|^2}{\left\|\mathbf{F}_m\mathbf{H}_{\text{BR}}\mathbf{a}_U\left(\Omega,\omega,r\right)\right\|_2^2} \right\}, \quad (43)$$

$$\widehat{g} = \frac{\left(\mathbf{y}^H\mathbf{F}_m\mathbf{H}_{\text{BR}}\mathbf{a}_U\left(\widehat{\Omega},\widehat{\omega},\widehat{r}\right)\right)^*}{\sqrt{P_p}\left\|\mathbf{F}_m\mathbf{H}_{\text{BR}}\mathbf{a}_U\left(\widehat{\Omega},\widehat{\omega},\widehat{r}\right)\right\|_2^2}, \quad (44)$$

where $\mathbf{a}_U(\Omega,\omega,r)$ is the near-field UPA steering vector [6]. Similar to the ULA RIS, we solve (43) numerically to obtain $\widehat{\Omega}$, $\widehat{r}$, and $\widehat{\omega}$. We use a three-dimensional grid of size $G_\Omega \times G_r \times G_\omega$, where G_Ω, G_r, and G_ω are the grid sizes for $\Omega \in [-1,1]$, $r \in [r_{\min}, r_{\max}]$, and, $\omega \in [-1,1]$, respectively. We set $G_\Omega = G_\omega = 10$ and $G_r = 7$. For the UPA RIS, to estimate the cascaded channel gain in (13) and the power allocation in Theorem 3, we obtain μ_{eq} and σ_{eq}^2 from Monte Carlo simulations with 10^4 realizations of g and noise. We set $\Omega = \omega = 0.5$ and $r = 20$ m.

Fig. 10(a) plots the achievable rate for a ULA RIS as a function of the normalized data power-to-noise ratio $P_d\sigma_g^2\left|\rho_{\text{BR}}\right|^2/\left(N\sigma_u^2\right)$ for two values of Υ_{UE}. Fig. 10(b) plots the respective results for the UPA RIS. The achievable rate trends for the UPA and ULA RISs are qualitatively similar. In both figures, as $P_d\sigma_g^2\left|\rho_{\text{BR}}\right|^2/\left(N\sigma_u^2\right)$ increases, the rate initially increases as the pilot-to-noise ratio increases. However, the rate then decreases. This is because less power is left for the downlink pilot, which leads to larger channel estimation errors and a lower SINR. In both figures, the achievable rate increases as Υ_{UE} increases because the MSE in estimating $\mathbf{h}_{\text{RU}}$ decreases. The power allocation obtained from Theorem 3 is within 1% of that obtained from simulations.

VI. CONCLUSIONS

We studied a parametric estimation scheme when the user was in the near-field of the RIS. We analyzed the impact of the

errors in estimating the RIS-to-user channel gain parameters, which were used to estimate the RIS-to-user channel gain and set the RIS configuration, and the cascaded channel gain on the achievable rate. We did this with the help of novel expressions for the CRLB on the estimation error of the directional cosine, the complex gain, and the distance, and a novel, tractable approximation for the cascaded channel gain. We also obtained the CRLB of the RIS-to-user channel gain. We presented an expression for the achievable rate in terms of the deterministic effective SINR, which captured the cumulative effect of the estimation errors on the RIS phase configuration and on coherent data demodulation. This led to insightful closed-form expressions for the optimal data and pilot powers.

While our analysis used asymptotic tools, our results applied for normalized energy budgets as small as -5 dB. The optimal number of pilots was less than the number of RIS elements, but was more than the number of estimated parameters. Furthermore, the optimal pilot power was more than the optimal data power. The proposed scheme had a higher achievable rate and a lower NMSE than the far-field, codebook-based, non-parametric, OMP, and EPA schemes.

An interesting avenue for future work is generalizing our analysis to compressed sensing algorithms for the near-field multi-cluster-based channel model. It is also of interest to analyze the impact of hardware imperfections and phase noise at the RIS and the impact of errors in estimating the AP-to-RIS channel gain.

APPENDIX

A. Proof of Lemma 1

It can be easily checked from (8) that the regularity conditions $\mathbb{E}_{\mathbf{y}}\left[\frac{\partial}{\partial u}\ln\left(f\left(\mathbf{y}|\,g,\Omega,r\right)\right)\big|\,g,\Omega,r\right]=0,\ \forall u\in\{g,\Omega,r\}$, for the existence of CRLB are satisfied. The CRLB $\mathbf{C}_{\text{CRLB}}(g,\Omega,r)$ is given by $\mathbf{J}^{-1}$, where $\mathbf{J}$ is the Fisher information matrix and is given by

$$\mathbf{J}=\begin{bmatrix} J_{gg} & J_{g\Omega} & J_{gr}\\ J_{g\Omega}^{*} & J_{\Omega\Omega} & J_{\Omega r}\\ J_{gr}^{*} & J_{\Omega r} & J_{rr}\end{bmatrix}. \tag{45}$$

Here, for $u,v\in\{g,\Omega,r\}$, we have

$$J_{uv}\triangleq\mathbb{E}_{\mathbf{y}}\left[\left(\frac{\partial}{\partial u}\ln\left(f\left(\mathbf{y}|\,g,\Omega,r\right)\right)\right)\times\left(\frac{\partial}{\partial v}\ln\left(f\left(\mathbf{y}|\,g,\Omega,r\right)\right)\right)^{*}\Bigg|\,g,\Omega,r\right]. \tag{46}$$

From (8), we can show that

$$\frac{\partial}{\partial g}\ln\left(f\left(\mathbf{y}|\,g,\Omega,r\right)\right)=\frac{1}{\sigma_{\text{AP}}^{2}}\left(\sqrt{P_p}\mathbf{y}^{H}\boldsymbol{\partial}_g-P_p g^{*}\left\|\boldsymbol{\partial}_g\right\|_2^2\right), \tag{47}$$

$$\frac{\partial}{\partial\Omega}\ln\left(f\left(\mathbf{y}|\,g,\Omega,r\right)\right)=\frac{2}{\sigma_{\text{AP}}^{2}}\Re\left\{g\sqrt{P_p}\mathbf{y}^{H}\boldsymbol{\partial}_{\Omega}-P_p\left|g\right|^{2}\boldsymbol{\partial}_g^{H}\boldsymbol{\partial}_{\Omega}\right\}, \tag{48}$$

$$\frac{\partial}{\partial r}\ln\left(f\left(\mathbf{y}|\,g,\Omega,r\right)\right)=\frac{2}{\sigma_{\text{AP}}^{2}}\Re\left\{g\mathbf{y}^{H}\boldsymbol{\partial}_r-P_p\left|g\right|^{2}\boldsymbol{\partial}_g^{H}\boldsymbol{\partial}_r\right\}. \tag{49}$$

Substituting (47), (48), and (49) in (46), and finding $\mathbf{J}^{-1}$ yields (17). We skip the algebraic details.

B. Brief Proof of Lemma 2

$\mathbf{C}_{\text{CRLB}}\left(\mathbf{h}_{\text{RU}}\right)\in\mathbb{C}^{N\times N}$ of $\mathbf{h}_{\text{RU}}=g\mathbf{b}(\Omega,r)$ can be written in terms of $\mathbf{C}_{\text{CRLB}}(g,\Omega,r)$ as follows [14, (3.30)]:

$$\mathbf{C}_{\text{CRLB}}\left(\mathbf{h}_{\text{RU}}\right)=\mathbf{J}_{\mathbf{h}_{\text{RU}}}\mathbf{C}_{\text{CRLB}}(g,\Omega,r)\mathbf{J}_{\mathbf{h}_{\text{RU}}}^{H}, \tag{50}$$

where $\mathbf{J}_{\mathbf{h}_{\text{RU}}}\triangleq\left[\frac{\partial\mathbf{h}_{\text{RU}}}{\partial g},\ \frac{\partial\mathbf{h}_{\text{RU}}}{\partial\Omega},\ \frac{\partial\mathbf{h}_{\text{RU}}}{\partial r}\right]\in\mathbb{C}^{N\times 3}$. Using $\mathbf{h}_{\text{RU}}=g\mathbf{b}(\Omega,r)$, it can be shown that $\frac{\partial\mathbf{h}_{\text{RU}}}{\partial g}=\mathbf{b}(\Omega,r)$, $\frac{\partial\mathbf{h}_{\text{RU}}}{\partial\Omega}=g\mathbf{b}(\Omega,r)\odot\mathbf{x}_{\Omega}$, and $\frac{\partial\mathbf{h}_{\text{RU}}}{\partial r}=g\mathbf{b}(\Omega,r)\odot\mathbf{x}_{r}$. Substituting these and $\mathbf{h}_{\text{RU}}=g\mathbf{b}(\Omega,r)$ yields $\mathbf{J}_{\mathbf{h}_{\text{RU}}}$ in (25).

C. Proof of Theorem 1

Let $\zeta_n\left(\widehat{g},\widehat{\Omega},\widehat{r}\right)\triangleq\frac{\widehat{\mathbf{h}}_{\text{RU}}^{*}[n]}{\left|\widehat{\mathbf{h}}_{\text{RU}}[n]\right|}=\frac{\widehat{g}^{*}}{|\widehat{g}|}\sqrt{N}\mathbf{b}^{*}\left(\widehat{\Omega},\widehat{r}\right)[n]$. Its first-order Taylor series expansion is given by

$$\zeta_n\left(\widehat{g},\widehat{\Omega},\widehat{r}\right)=\zeta_n\left(g,\Omega,r\right)-\nabla\zeta_n^{T}\left(g,\Omega,r\right)\mathbf{e}_l+\delta_{\text{rem}}, \tag{51}$$

where δ_{rem} is the remainder term and $\nabla\zeta_n\left(g,\Omega,r\right)$ is the gradient of $\zeta_n\left(\widehat{g},\widehat{\Omega},\widehat{r}\right)$ evaluated at g, Ω, and r.

First we evaluate $\nabla\zeta_n\left(g,\Omega,r\right)$. From (1), we get

$$\frac{\partial}{\partial\widehat{g}}\zeta_n\left(\widehat{g},\widehat{\Omega},\widehat{r}\right)=-\frac{\left(\widehat{g}^{*}\right)^{2}}{2\left|\widehat{g}\right|^{3}}\sqrt{N}\mathbf{b}^{*}\left(\widehat{\Omega},\widehat{r}\right)[n], \tag{52}$$

$$\frac{\partial}{\partial\widehat{\Omega}}\zeta_n\left(\widehat{g},\widehat{\Omega},\widehat{r}\right)=-\frac{\widehat{g}^{*}}{|\widehat{g}|}\sqrt{N}\mathbf{b}^{*}\left(\widehat{\Omega},\widehat{r}\right)[n]\times\left(j\frac{2\pi\left(n-1\right)}{\lambda}\left[d+\frac{\widehat{\Omega}}{\widehat{r}}\left(n-1\right)d^{2}\right]\right), \tag{53}$$

$$\frac{\partial}{\partial\widehat{r}}\zeta_n\left(\widehat{g},\widehat{\Omega},\widehat{r}\right)=-\frac{\widehat{g}^{*}}{|\widehat{g}|}\sqrt{N}\mathbf{b}^{*}\left(\widehat{\Omega},\widehat{r}\right)[n]\times\left(j\frac{\pi}{\lambda}\left[\frac{1}{\widehat{r}^{2}}\left(n-1\right)^{2}d^{2}\left(1-\widehat{\Omega}^{2}\right)\right]\right). \tag{54}$$

Combining (52), (53), and (54), we get

$$\nabla\zeta_n\left(g,\Omega,r\right)=-\frac{g^{*}}{|g|}\sqrt{N}\mathbf{b}^{*}\left(\Omega,r\right)[n]\,\boldsymbol{\eta}_n\left(g,\Omega,r\right), \tag{55}$$

where $\boldsymbol{\eta}_n\left(g,\Omega,r\right)\triangleq\left[\frac{g^{*}}{2|g|^{2}},\ \mathbf{x}_{\Omega}[n],\ \mathbf{x}_{r}[n]\right]^{T}$.

Next, we evaluate the remainder term in (51) given by $\delta_{\text{rem}}=\frac{1}{2}\mathbf{e}_l^{T}\nabla^{2}\zeta_n\left(g',\Omega',r'\right)\mathbf{e}_l$. Here, $\nabla^{2}\zeta_n\left(g',\Omega',r'\right)$ is the Hessian of $\zeta_n\left(\widehat{g},\widehat{\Omega},\widehat{r}\right)$ evaluated at g', Ω', and r'. Conditioned on g, Ω, and r, $\mathbf{e}_l\sim\mathcal{CN}\left(\mathbf{0},\mathbf{C}_{\text{CRLB}}(g,\Omega,r)\right)$. From (17), we get $\mathbf{C}_{\text{CRLB}}(g,\Omega,r)\to\mathbf{0}$ as $P_p/\sigma_{\text{AP}}^{2}\to\infty$. Therefore, $\mathbf{e}_l\to\mathbf{0}$ as $P_p/\sigma_{\text{AP}}^{2}\to\infty$ and δ_{rem} decays as $o\left(\sigma_{\text{AP}}/\sqrt{P_p}\right)$.

Substituting (51) and (55) in (5) and simplifying yields (26).

D. Proof of Lemma 3

We derive expressions for μ_{eq} and σ_{eq}^{2} separately below.

a) μ_{eq}: From the law of iterated expectations, we have $\mu_{\text{eq}} = \mathbb{E}\left[\mathbb{E}_{\mathbf{e}_l}\left[h_{\text{eq}}\left(\widehat{\boldsymbol{\phi}},\Omega,r\right)\middle| g,\Omega,r\right]\right]$. From (26), we get

$$\mathbb{E}_{\mathbf{e}_l}\left[h_{\text{eq}}\left(\widehat{\boldsymbol{\phi}},\Omega,r\right)\middle| g,\Omega,r\right] = \frac{|g|}{\sqrt{N}}\left\|\mathbf{h}_{\text{BR}}\right\|_1 + \frac{|g|}{\sqrt{N}}\sum_{n=1}^{N}\left|\mathbf{h}_{\text{BR}}[n]\right|\boldsymbol{\eta}_n^T(g,\Omega,r)\,\mathbb{E}\left[\mathbf{e}_l\middle| g,\Omega,r\right]. \quad (56)$$

Since $\mathbb{E}\left[\mathbf{e}_l\middle| g,\Omega,r\right] = \mathbf{0}$, we get $\mu_{\text{eq}} = \mathbb{E}\left[|g|\right]\left\|\mathbf{h}_{\text{BR}}\right\|_1/\sqrt{N}$. Since $g \sim \mathcal{CN}\left(0,\sigma_g^2\right)$, $|g|$ is Rayleigh distributed with mean $\mathbb{E}\left[|g|\right] = \sqrt{0.25\pi\sigma_g^2}$. Substituting this in μ_{eq} yields (28).

b) σ_{eq}^2: We can write the second moment of $h_{\text{eq}}\left(\widehat{\boldsymbol{\phi}},\Omega,r\right)$ as

$$\mathbb{E}\left[\left|h_{\text{eq}}\left(\widehat{\boldsymbol{\phi}},\Omega,r\right)\right|^2\right] = \mathbb{E}\left[\mathbb{E}_{\mathbf{e}_l}\left[\left|h_{\text{eq}}\left(\widehat{\boldsymbol{\phi}},\Omega,r\right)\right|^2\middle| g,\Omega,r\right]\right]. \quad (57)$$

As above, after substituting (26), we get

$$\mathbb{E}_{\mathbf{e}_l}\left[\left|h_{\text{eq}}\left(\widehat{\boldsymbol{\phi}},\Omega,r\right)\right|^2\middle| g,\Omega,r\right] = \frac{|g|^2}{N}\left\|\mathbf{h}_{\text{BR}}\right\|_1^2 + \frac{2|g|^2}{N}\left\|\mathbf{h}_{\text{BR}}\right\|_1\sum_{n=1}^{N}\left|\mathbf{h}_{\text{BR}}[n]\right|\Re\left\{\boldsymbol{\eta}_n^T(g,\Omega,r)\,\mathbb{E}_{\mathbf{e}_l}\left[\mathbf{e}_l\middle| g,\Omega,r\right]\right\} + \frac{|g|^2}{N}\sum_{n=1}^{N}\sum_{m=1}^{N}\left|\mathbf{h}_{\text{BR}}[n]\right|\left|\mathbf{h}_{\text{BR}}[m]\right| \times \boldsymbol{\eta}_n^T(g,\Omega,r)\,\mathbb{E}_{\mathbf{e}_l}\left[\mathbf{e}_l\mathbf{e}_l^H\middle| g,\Omega,r\right]\boldsymbol{\eta}_m^*(g,\Omega,r). \quad (58)$$

For large M, conditioned on g, Ω, and r, we know that $\mathbf{e}_l \sim \mathcal{CN}\left(\mathbf{0},\mathbf{C}_{\text{CRLB}}(g,\Omega,r)\right)$. Hence,

$$\mathbb{E}\left[\left|h_{\text{eq}}\left(\widehat{\boldsymbol{\phi}},\Omega,r\right)\right|^2\middle| g,\Omega,r\right] = \frac{|g|^2}{N}\left\|\mathbf{h}_{\text{BR}}\right\|_1^2 + \frac{|g|^2}{N}\sum_{n,m=1}^{N}\left|\mathbf{h}_{\text{BR}}[n]\right| \times \left|\mathbf{h}_{\text{BR}}[m]\right|\boldsymbol{\eta}_n^T(g,\Omega,r)\,\mathbf{C}_{\text{CRLB}}(g,\Omega,r)\boldsymbol{\eta}_m^*(g,\Omega,r). \quad (59)$$

Substituting (59) in (57), we get

$$\mathbb{E}\left[\left|h_{\text{eq}}\left(\widehat{\boldsymbol{\phi}},\Omega,r\right)\right|^2\right] = \frac{\sigma_g^2}{N}\left\|\mathbf{h}_{\text{BR}}\right\|_1^2 + \sum_{n,m=1}^{N}\left|\mathbf{h}_{\text{BR}}[n]\right|\left|\mathbf{h}_{\text{BR}}[m]\right| \times \frac{1}{N}\mathbb{E}\left[|g|^2\boldsymbol{\eta}_n^T(g,\Omega,r)\,\mathbf{C}_{\text{CRLB}}(g,\Omega,r)\boldsymbol{\eta}_m^*(g,\Omega,r)\right]. \quad (60)$$

From (17), the last line in (60) can be shown to reduce to

$$\mathbb{E}\left[|g|^2\boldsymbol{\eta}_n^T(g,\Omega,r)\,\mathbf{C}_{\text{CRLB}}(g,\Omega,r)\boldsymbol{\eta}_m^*(g,\Omega,r)\right] = \frac{\sigma_{\text{AP}}^2}{P_p}\left(\delta_{nm} + \mathbb{E}\left[e^{j2\theta_g}\right]\frac{j\pi}{\lambda}\gamma_n - \mathbb{E}\left[e^{-j2\theta_g}\right]\frac{j\pi}{\lambda}\gamma_m^*\right), \quad (61)$$

where $\theta_g = \angle g$, δ_{nm} is given in (30), and $\gamma_m = \frac{\beta_{g\Omega}(m-1)d}{2}\left(1+\frac{\Omega}{r}d(m-1)\right) + \frac{\beta_{gr}\left(1-\Omega^2\right)(m-1)^2d^2}{4r^2}$.

As g is circularly symmetric, θ_g is uniformly distributed over $[-\pi,\pi]$ and $\mathbb{E}\left[e^{\pm j2\theta_g}\right] = 0$. Substituting in (60), we get

$$\mathbb{E}\left[\left|h_{\text{eq}}\left(\widehat{\boldsymbol{\phi}},\Omega,r\right)\right|^2\right] = \frac{\sigma_g^2}{N}\left\|\mathbf{h}_{\text{BR}}\right\|_1^2 + \frac{\sigma_{\text{AP}}^2}{P_pN}\sum_{n=1}^{N}\sum_{m=1}^{N}\left|\mathbf{h}_{\text{BR}}[n]\right|\left|\mathbf{h}_{\text{BR}}[m]\right|\delta_{nm}. \quad (62)$$

Substituting (28) and (62) in the formula $\sigma_{\text{eq}}^2 = \mathbb{E}\left[\left|h_{\text{eq}}\left(\widehat{\boldsymbol{\phi}},\Omega,r\right)\right|^2\right] - \left|\mu_{\text{eq}}\right|^2$ yields (29).

E. Proof of Theorem 2

The achievable rate is given by [35, (15)]

$$R = \left(1-\frac{M+1}{T_c}\right)\mathbb{E}\left[\log_2\left(1+\frac{P_d\left|\widehat{h}_{\text{eq}}\left(\widehat{\boldsymbol{\phi}};\Omega,r\right)\right|^2}{P_d\mathbb{E}\left[\left|e_{\text{eq}}\right|^2\right]+\sigma_u^2}\right)\right]. \quad (63)$$

Here, the term $\left(1-[M+1]/T_c\right)$ arises as $T_c - M - 1$ symbol durations out of T_c symbol durations are available for data transmission.

Let $\Gamma_{\text{eff}}(P_p,P_c,P_d) \triangleq \frac{P_d\mathbb{E}\left[\left|\widehat{h}_{\text{eq}}\left(\widehat{\boldsymbol{\phi}};\Omega,r\right)\right|^2\right]}{P_d\mathbb{E}\left[\left|e_{\text{eq}}\right|^2\right]+\sigma_u^2}$ and $\widetilde{h}_{\text{eq}}\left(\widehat{\boldsymbol{\phi}}\right) = \frac{\widehat{h}_{\text{eq}}\left(\widehat{\boldsymbol{\phi}};\Omega,r\right)}{\sqrt{\mathbb{E}\left[\left|\widehat{h}_{\text{eq}}\left(\widehat{\boldsymbol{\phi}};\Omega,r\right)\right|^2\right]}}$. Substituting these in (63) yields (35). From [14, (12.8)], we get

$$\mathbb{E}\left[\left|e_{\text{eq}}\right|^2\right] = \sigma_{\text{eq}}^2 - \frac{P_c\sigma_{\text{eq}}^4}{P_c\sigma_{\text{eq}}^2+\sigma_u^2} = \frac{\sigma_{\text{eq}}^2\sigma_u^2}{P_c\sigma_{\text{eq}}^2+\sigma_u^2}. \quad (64)$$

And, from (13), we get

$$\mathbb{E}\left[\left|\widehat{h}_{\text{eq}}\left(\widehat{\boldsymbol{\phi}};\Omega,r\right)\right|^2\right] = \left|\mu_{\text{eq}}\right|^2 + \frac{P_c\sigma_{\text{eq}}^4}{P_c\sigma_{\text{eq}}^2+\sigma_u^2}. \quad (65)$$

Substituting (64) and (65) in $\Gamma_{\text{eff}}(P_p,P_c,P_d)$ yields (36).

F. Proof of Corollary 2

Let $e_{\text{eff}} \triangleq \widetilde{h}_{\text{eq}}\left(\widehat{\boldsymbol{\phi}}\right) - \frac{h_{\text{eq}}\left(\boldsymbol{\phi}^{\text{opt}}\right)}{\sqrt{\mathbb{E}\left[\left|h_{\text{eq}}\left(\boldsymbol{\phi}^{\text{opt}}\right)\right|^2\right]}}$. Then, R in (35) is

$$R = \left(1-\frac{M+1}{T_c}\right)\mathbb{E}\Big[\log_2\left(1+\Gamma_{\text{eff}}(P_p,P_c,P_d)\right) \times \left|\left(\mathbb{E}\left[\left|h_{\text{eq}}\left(\boldsymbol{\phi}^{\text{opt}}\right)\right|^2\right]\right)^{-\frac{1}{2}}h_{\text{eq}}\left(\boldsymbol{\phi}^{\text{opt}}\right)+e_{\text{eff}}\right|^2\right)\Big]. \quad (66)$$

We first derive an expression for $\mathbb{E}\left[\left|e_{\text{eff}}\right|^2\right]$ and characterize its asymptotic behavior.

Lemma 4. *$\mathbb{E}\left[\left|e_{eff}\right|^2\right] = o\left(\sigma_{AP}^2/\left(P_p\sigma_g^2\right)\right)$ for large $P_c\sigma_g^2/\sigma_u^2$ and $P_p\sigma_g^2/\sigma_{AP}^2$.*

Proof: Substituting (37) in $\mathbb{E}\left[\left|e_{\text{eff}}\right|^2\right]$, we get

$$\mathbb{E}\left[\left|e_{\text{eff}}\right|^2\right] = 2 - \frac{2\Re\left\{\varsigma_{\text{eq}}\right\}}{\sqrt{\mathbb{E}\left[\left|h_{\text{eq}}\left(\boldsymbol{\phi}^{\text{opt}}\right)\right|^2\right]\mathbb{E}\left[\left|\widehat{h}_{\text{eq}}\left(\widehat{\boldsymbol{\phi}};\Omega,r\right)\right|^2\right]}}. \quad (67)$$

where $\varsigma_{\text{eq}} = \mathbb{E}\left[\widehat{h}_{\text{eq}}^*\left(\widehat{\boldsymbol{\phi}};\Omega,r\right)h_{\text{eq}}\left(\boldsymbol{\phi}^{\text{opt}}\right)\right]$. From (6) and (13), we can write ς_{eq} as

$$\varsigma_{\text{eq}} = \mathbb{E}\left[h_{\text{eq}}\left(\boldsymbol{\phi}^{\text{opt}}\right)\left(\mu_{\text{eq}}^{*} - \frac{\mu_{\text{eq}}^{*} P_c \sigma_{\text{eq}}^2}{P_c\sigma_{\text{eq}}^2+\sigma_u^2} + \frac{P_c\sigma_{\text{eq}}^2 h_{\text{eq}}^{*}\left(\widehat{\mathbf{h}}_{\text{RU}}\right)}{P_c\sigma_{\text{eq}}^2+\sigma_u^2}\right)\right] + \frac{\sqrt{P_c}\sigma_{\text{eq}}^2}{P_c\sigma_{\text{eq}}^2+\sigma_u^2}\mathbb{E}\left[h_{\text{eq}}\left(\boldsymbol{\phi}^{\text{opt}}\right) n_u^{*}\right]. \quad (68)$$

From (27), $\mathbb{E}\left[h_{\text{eq}}\left(\boldsymbol{\phi}^{\text{opt}}\right)\right] = \mu_{\text{eq}}$. Since n_u is zero-mean and is independent of $h_{\text{eq}}\left(\boldsymbol{\phi}^{\text{opt}}\right)$, $\mathbb{E}\left[h_{\text{eq}}\left(\boldsymbol{\phi}^{\text{opt}}\right) n_u^{*}\right] = 0$. Substituting these in (68), we get

$$\varsigma_{\text{eq}} = \frac{\sigma_u^2\left|\mu_{\text{eq}}\right|^2 + P_c\sigma_{\text{eq}}^2\mathbb{E}\left[h_{\text{eq}}\left(\boldsymbol{\phi}^{\text{opt}}\right) h_{\text{eq}}^{*}\left(\widehat{\mathbf{h}}_{\text{RU}}\right)\right]}{P_c\sigma_{\text{eq}}^2+\sigma_u^2}. \quad (69)$$

Using law of iterated expectations, we get

$$\mathbb{E}\left[h_{\text{eq}}\left(\boldsymbol{\phi}^{\text{opt}}\right) h_{\text{eq}}^{*}\left(\widehat{\mathbf{h}}_{\text{RU}}\right)\right] = \mathbb{E}\left[\mathbb{E}_{\mathbf{e}_l}\left[h_{\text{eq}}\left(\boldsymbol{\phi}^{\text{opt}}\right) h_{\text{eq}}^{*}\left(\widehat{\mathbf{h}}_{\text{RU}}\right)\middle| g,\Omega,r\right]\right]. \quad (70)$$

From (26) and (27), we have $h_{\text{eq}}\left(\widehat{\boldsymbol{\phi}},\Omega,r\right) = h_{\text{eq}}\left(\boldsymbol{\phi}^{\text{opt}}\right) + \frac{|g|}{\sqrt{N}}\sum_{n=1}^{N}\mathbf{h}_{\text{BR}}[n]\,\boldsymbol{\eta}_n^{T}(g,\Omega,r)\,\mathbf{e}_l$. Substituting this, we get

$$\mathbb{E}\left[h_{\text{eq}}\left(\boldsymbol{\phi}^{\text{opt}}\right) h_{\text{eq}}^{*}\left(\widehat{\mathbf{h}}_{\text{RU}}\right)\right] = \mathbb{E}\left[\left|h_{\text{eq}}\left(\boldsymbol{\phi}^{\text{opt}}\right)\right|^2\right] + \mathbb{E}\left[\frac{|g|}{\sqrt{N}} \times h_{\text{eq}}\left(\boldsymbol{\phi}^{\text{opt}}\right)\sum_{n=1}^{N}\mathbf{h}_{\text{BR}}^{*}[n]\,\boldsymbol{\eta}_n^{H}(g,\Omega,r)\,\mathbb{E}_{\mathbf{e}_l}\left[\mathbf{e}_l^{*}\middle| g,\Omega,r\right]\right]. \quad (71)$$

Since $\mathbb{E}_{\mathbf{e}_l}\left[\mathbf{e}_l^{*}|g,\Omega,r\right] = 0$, (71) simplifies to $\mathbb{E}\left[h_{\text{eq}}\left(\boldsymbol{\phi}^{\text{opt}}\right) h_{\text{eq}}^{*}\left(\widehat{\mathbf{h}}_{\text{RU}}\right)\right] = \mathbb{E}\left[\left|h_{\text{eq}}\left(\boldsymbol{\phi}^{\text{opt}}\right)\right|^2\right]$. Substituting this in (69) and simplifying yields

$$\varsigma_{\text{eq}} = \frac{\left|\mu_{\text{eq}}\right|^2\sigma_u^2 + P_c\sigma_{\text{eq}}^2\mathbb{E}\left[\left|h_{\text{eq}}\left(\boldsymbol{\phi}^{\text{opt}}\right)\right|^2\right]}{P_c\sigma_{\text{eq}}^2+\sigma_u^2}. \quad (72)$$

Finally, substituting (72) in (67), we get

$$\mathbb{E}\left[\left|e_{\text{eff}}\right|^2\right] = 2 - \frac{\frac{2|\mu_{\text{eq}}|^2\sigma_u^2}{P_c\sigma_{\text{eq}}^2+\sigma_u^2} + \frac{P_c\sigma_{\text{eq}}^2\mathbb{E}\left[\left|h_{\text{eq}}\left(\boldsymbol{\phi}^{\text{opt}}\right)\right|^2\right]}{P_c\sigma_{\text{eq}}^2+\sigma_u^2}}{\sqrt{\mathbb{E}\left[\left|h_{\text{eq}}\left(\boldsymbol{\phi}^{\text{opt}}\right)\right|^2\right]\mathbb{E}\left[\left|\widehat{h}_{\text{eq}}\left(\widehat{\boldsymbol{\phi}};\Omega,r\right)\right|^2\right]}}. \quad (73)$$

From (29), we can show for large $P_c\sigma_g^2/\sigma_u^2$ and $P_p\sigma_g^2/\sigma_{\text{AP}}^2$ that $\frac{\sigma_u^2}{P_c\sigma_{\text{eq}}^2+\sigma_u^2} \to 0$ and $\frac{\mathbb{E}\left[\left|h_{\text{eq}}\left(\boldsymbol{\phi}^{\text{opt}}\right)\right|^2\right]}{\sqrt{\mathbb{E}\left[\left|h_{\text{eq}}\left(\boldsymbol{\phi}^{\text{opt}}\right)\right|^2\right]\mathbb{E}\left[\left|\widehat{h}_{\text{eq}}\left(\widehat{\boldsymbol{\phi}};\Omega,r\right)\right|^2\right]}} = 1 + o\left(\sigma_{\text{AP}}^2/\left(P_p\sigma_g^2\right)\right)$. Hence, $\mathbb{E}\left[\left|e_{\text{eff}}\right|^2\right] = o\left(\sigma_{\text{AP}}^2/\left(P_p\sigma_g^2\right)\right)$. ■

Thus, as $P_p\sigma_g^2/\sigma_{\text{AP}}^2$ and $P_c\sigma_g^2/\sigma_u^2 \to \infty$, $\mathbb{E}\left[\left|e_{\text{eff}}\right|^2\right] = 0$. Hence, e_{eff} converges to 0 in the mean-squared sense. Mean-squared convergence implies convergence in distribution [36, Th. 7.2.3]. Let

$$a(x) \triangleq \left(1 - \frac{M+1}{T_c}\right)\mathbb{E}\Big[\log_2\left(1+\Gamma_{\text{eff}}\left(P_p,P_c,P_d\right)\right. \times\left.\left|\left(\mathbb{E}\left[\left|h_{\text{eq}}\left(\boldsymbol{\phi}^{\text{opt}}\right)\right|^2\right]\right)^{-\frac{1}{2}} h_{\text{eq}}\left(\boldsymbol{\phi}^{\text{opt}}\right) + x\right|^2\right)\Big]. \quad (74)$$

$a(x)$ is a continuous function of x. Therefore using [36, Th. 7.2.18], $a\left(e_{\text{eff}}\right) \to a(0)$ in distribution as $P_p\sigma_g^2/\sigma_{\text{AP}}^2$ and $P_c\sigma_g^2/\sigma_u^2 \to \infty$. Using the Jensen's inequality and simplifying further, we can show that $R = \mathbb{E}\left[a\left(e_{\text{eff}}\right)\right]$ and $\widetilde{R} = \mathbb{E}\left[a(0)\right]$ are upper bounded by $\left(1-[M+1]/T_c\right)\log_2\left(1+\Gamma_{\text{eff}}\left(P_p,P_c,P_d\right)\right)$. Hence, $R \to \widetilde{R}$. Finally, substituting $\frac{h_{\text{eq}}\left(\boldsymbol{\phi}^{\text{opt}}\right)}{\sqrt{\mathbb{E}\left[\left|h_{\text{eq}}\left(\boldsymbol{\phi}^{\text{opt}}\right)\right|^2\right]}} = g/\sigma_g$ in $\widetilde{R}$ yields (38).

G. Proof of Theorem 3

At the optimal values, the constraints in (39b) and (39c) must be met with equality. Therefore, the optimal user power $P_p^{\star}$ is $E_{\text{UE}}/\left(T_s M\right)$ and $P_c^{\star}(\Omega,r) + (T_c - M - 1)\,P_d^{\star}(\Omega,r) = E_{\text{AP}}/T_s$. Substituting $P_c = \left(E_{\text{AP}}/T_s\right) - (T_c - M - 1)P_d$ and simplifying, $\Gamma_{\text{eff}}\left(P_d\right)$ in (39a) is given by

$$\Gamma_{\text{eff}}\left(P_d\right) = \frac{P_d u_1 - P_d^2 u_2}{u_4 - P_d u_3}, \quad (75)$$

where $u_1 \triangleq E_{\text{AP}}\sigma_{\text{eq}}^2\left(\left|\mu_{\text{eq}}\right|^2+\sigma_{\text{eq}}^2\right)/T_s + \left(\left|\mu_{\text{eq}}\right|^2\sigma_u^2\right)$, $u_2 \triangleq (T_c - M - 1)\sigma_{\text{eq}}^2\left(\left|\mu_{\text{eq}}\right|^2+\sigma_{\text{eq}}^2\right)$, $u_3 \triangleq (T_c - M - 2)\sigma_{\text{eq}}^2\sigma_u^2$, and $u_4 \triangleq \sigma_u^2\left(\left(E_{\text{AP}}\sigma_{\text{eq}}^2/T_s\right)+\sigma_u^2\right)$.

From (75), we can show that $\frac{\partial\Gamma_{\text{eff}}(P_d)}{\partial P_d} = \left(u_2u_3P_d^2 - 2u_2u_4P_d + u_1u_4\right)/\left(u_4 - P_d u_3\right)^2$. Hence, the solution of $\frac{\partial\Gamma_{\text{eff}}(P_d)}{\partial P_d} = 0$ is

$$P_d^{\star}(\Omega,r) = \frac{u_2u_4 \pm \sqrt{u_2^2u_4^2 - u_1u_2u_3u_4}}{u_2u_3}. \quad (76)$$

Among the two possibilities, the second derivative of $\Gamma_{\text{eff}}\left(P_d\right)$ evaluated at $P_d^{\star}(\Omega,r) = \left(u_2u_4 + \sqrt{u_2^2u_4^2 - u_1u_2u_3u_4}\right)/\left(u_2u_3\right)$ is positive, which rules out this root as the optimal solution. Hence, $P_d^{\star}(\Omega,r) = \left(u_2u_4 - \sqrt{u_2^2u_4^2 - u_1u_2u_3u_4}\right)/\left(u_2u_3\right)$. Substituting the expressions of u_1, u_2, u_3, and u_4 in this yields (41).

REFERENCES

[1] S. Dhok and N. B. Mehta, "Parametric channel estimation for near-field RIS configuration and data demodulation," *To appear in Proc. IEEE Global Commun. Conf. (GLOBECOM)*, Dec. 2025.

[2] M. Cui, Z. Wu, Y. Lu, X. Wei, and L. Dai, "Near-field MIMO communications for 6G: Fundamentals, challenges, potentials, and future directions," *IEEE Commun. Mag.*, vol. 61, no. 1, pp. 40–46, Jan. 2023.

[3] H. Zhang, N. Shlezinger, F. Guidi, D. Dardari, and Y. C. Eldar, "6G wireless communications: From far-field beam steering to near-field beam focusing," *IEEE Commun. Mag.*, vol. 61, no. 4, pp. 72–77, Apr. 2023.

[4] Y. Liu, Z. Wang, J. Xu, C. Ouyang, X. Mu, and R. Schober, "Near-field communications: A tutorial review," *IEEE Open J. Commun. Soc.*, vol. 4, pp. 1999–2049, 2023.

[5] Y. Pan, C. Pan, S. Jin, and J. Wang, "RIS-aided near-field localization and channel estimation for the terahertz system," *IEEE J. Sel. Topics Signal Process.*, vol. 17, no. 4, pp. 878–892, Jul. 2023.

[6] M. Haghshenas, P. Ramezani, M. Magarini, and E. Björnson, "Parametric channel estimation with short pilots in RIS-assisted near- and far-field communications," *IEEE Trans. Wireless Commun.*, vol. 23, no. 8, pp. 10 366–10 382, Aug. 2024.

[7] E. Björnson and P. Ramezani, "Maximum likelihood channel estimation for RIS-Aided communications with LOS channels," in *Proc. Asilomar Conf. Signals, Syst., Comput.*, Oct. 2022, pp. 403–407.

[8] S. Yang, C. Xie, W. Lyu, B. Ning, Z. Zhang, and C. Yuen, "Near-field channel estimation for extremely large-scale reconfigurable intelligent surface (XL-RIS)-aided wideband mmWave systems," *IEEE J. Sel. Areas Commun.*, vol. 42, no. 6, pp. 1567–1582, Jun. 2024.

[9] S. Yang, W. Lyu, Z. Hu, Z. Zhang, and C. Yuen, "Channel estimation for near-field XL-RIS-Aided mmWave hybrid beamforming architectures," *IEEE Trans. Veh. Technol.*, vol. 72, no. 8, pp. 11 029–11 034, Aug. 2023.

[10] J. Wu, S. Kim, and B. Shim, "Near-field channel estimation for RIS-Assisted wideband terahertz systems," in *Proc. IEEE Global Commun. Conf. (GLOBECOM)*, Dec. 2022, pp. 3893–3898.

[11] Y. Zhang, X. Wu, and C. You, "Fast near-field beam training for extremely large-scale array," *IEEE Wireless Commun. Lett.*, vol. 11, no. 12, pp. 2625–2629, Dec. 2022.

[12] S. Naduvilpattu and N. B. Mehta, "Optimal time and power allocation for phase-shift configuration and downlink channel estimation in RIS-aided systems," *IEEE Trans. Wireless Commun.*, vol. 23, no. 8, pp. 9419–9431, Aug. 2024.

[13] S. Ganesan, N. B. Mehta, and R. Sarvendranath, "A novel demodulation and selection pilot power trade-off for codebook-based IRS with imperfect channel estimates," in *Proc. IEEE Intl. Conf. Acoust., Speech Signal Process. (ICASSP)*, Apr. 2024, pp. 8876–8880.

[14] S. Kay, *Fundamentals of Statistical Signal Processing, Vol. 1: Estimation Theory*, 1st ed. Pearson Education, 1993.

[15] T.-J. Shan, M. Wax, and T. Kailath, "On spatial smoothing for direction-of-arrival estimation of coherent signals," *IEEE Trans. Acoust., Speech, Signal Process.*, vol. 33, no. 4, pp. 806–811, Aug. 1985.

[16] K. Muralidhar, M. Budavarapu, S. K. Das, and S. S. Rout, "Parametric estimation of rapidly varying channels in OFDM systems," in *Proc. IEEE Intl. Conf. Signal Process., Inform., Commun. Energy Syst.*, Feb. 2015, pp. 1–5.

[17] M. Cui and L. Dai, "Channel estimation for extremely large-scale MIMO: Far-field or near-field?" *IEEE Trans. Commun.*, vol. 70, no. 4, pp. 2663–2677, Apr. 2022.

[18] Y. Lu and L. Dai, "Near-field channel estimation in mixed LoS/NLoS environments for extremely large-scale MIMO systems," *IEEE Trans. Commun.*, vol. 71, no. 6, pp. 3694–3707, Jun. 2023.

[19] Q. Li, M. El-Hajjar, Y. Sun, and L. Hanzo, "Performance analysis of reconfigurable holographic surfaces in the near-field scenario of cell-free networks under hardware impairments," *IEEE Trans. Wireless Commun.*, vol. 23, no. 9, pp. 11 972–11 984, Sep. 2024.

[20] S. Foucart and H. Rauhut, *A Mathematical Introduction to Compressive Sensing*. Birkhäuser, 2013.

[21] F. Zhang, M.-M. Zhao, M. Lei, and M. Zhao, "Joint power allocation and phase-shift design for RIS-aided cooperative near-field localization," in *Proc. Intl. Symp. Wireless Commun. Syst.*, Oct. 2022, pp. 1–6.

[22] J. An, C. Xu, L. Wang, Y. Liu, L. Gan, and L. Hanzo, "Joint training of the superimposed direct and reflected links in reconfigurable intelligent surface assisted multiuser communications," *IEEE Trans. Green Commun. Netw.*, vol. 6, no. 2, pp. 739–754, Jun. 2022.

[23] W. Yang, M. Li, and Q. Liu, "A novel anchor-assisted channel estimation for RIS-aided multiuser communication systems," *IEEE Commun. Lett.*, vol. 26, no. 11, pp. 2740–2744, Nov. 2022.

[24] A. Taha, M. Alrabeiah, and A. Alkhateeb, "Enabling large intelligent surfaces with compressive sensing and deep learning," *IEEE Access*, vol. 9, pp. 44 304–44 321, 2021.

[25] W. Tang, M. Z. Chen, X. Chen, J. Y. Dai, Y. Han, M. Di Renzo, Y. Zeng, S. Jin, Q. Cheng, and T. J. Cui, "Wireless communications with reconfigurable intelligent surface: Path loss modeling and experimental measurement," *IEEE Trans. Wireless Commun.*, vol. 20, no. 1, pp. 421–439, Jan. 2021.

[26] B. Zheng and R. Zhang, "Intelligent reflecting surface-enhanced OFDM: Channel estimation and reflection optimization," *IEEE Wireless Commun. Lett.*, vol. 9, no. 4, pp. 518–522, Apr. 2020.

[27] B. Shamasundar, N. Daryanavardan, and A. Nosratinia, "Channel training & estimation for reconfigurable intelligent surfaces: Exposition of principles, approaches, and open problems," *IEEE Access*, vol. 11, pp. 6717–6734, 2023.

[28] J. An, L. Wang, C. Xu, L. Gan, and L. Hanzo, "Optimal pilot power based channel estimation improves the throughput of intelligent reflective surface assisted systems," *IEEE Trans. Veh. Technol.*, vol. 69, no. 12, pp. 16 202–16 206, Dec. 2020.

[29] D. Tse and P. Viswanath, *Fundamentals of Wireless Communication*. Cambridge University Press, 2005.

[30] J. Chambers, *Graphical Methods for Data Analysis*. CRC Press, 1983.

[31] R. A. Horn and C. R. Johnson, *Matrix Analysis*, 2nd ed. Cambridge Univ. Press, 2013.

[32] W. Chen, Z. Yang, Z. Wei, D. Wing Kwan Ng, and M. Matthaiou, "RIS-Aided MIMO beamforming: Piecewise near-field channel model," *IEEE Trans. Commun.*, vol. 73, no. 10, pp. 9612–9626, Oct. 2025.

[33] Q. Zhou, J. Zhao, K. Cai, and Y. Zhu, "RIS-assisted beamfocusing in near-field IoT communication systems: A transformer-based approach," *IEEE Internet Things J.*, vol. 12, no. 15, pp. 30 564–30 575, Aug. 2025.

[34] Y. Cheng, C. Huang, W. Peng, M. Debbah, L. Hanzo, and C. Yuen, "Achievable rate optimization of the RIS-Aided near-field wideband uplink," *IEEE Trans. Wireless Commun.*, vol. 23, no. 3, pp. 2296–2311, Mar. 2024.

[35] B. Hassibi and B. Hochwald, "How much training is needed in multiple-antenna wireless links?" *IEEE Trans. Inf. Theory*, vol. 49, no. 4, pp. 951–963, Apr. 2003.

[36] G. R. Grimmett and D. R. Stirzaker, *Probability and Random Process*. Oxford Univ. Press, 2001.

Shivani Dhok (Student Member, IEEE) Shivani Dhok received her B.Tech. in Electronics and Communication Engineering in the year 2021 from the Indian Institute of Information Technology, Nagpur, India. She is currently pursuing a Ph.D. with the Department of Electrical Communication Engineering, Indian Institute of Science (IISc), Bengaluru, India. She was awarded the Prime Minister's Research Fellowship (PMRF). Her research interests include wireless communication and signal processing for wireless communication.

Neelesh B. Mehta (Fellow, IEEE) received the B.Tech. degree in electronics and communications engineering from the Indian Institute of Technology (IIT) Madras in 1996 and the M.S. and Ph.D. degrees in electrical engineering from the California Institute of Technology, Pasadena, USA, in 1997 and 2001, respectively. He is currently a Professor and Chair of the Department of Electrical Communication Engineering, Indian Institute of Science, Bengaluru. He is a fellow of the Indian National Science Academy, Indian Academy of Sciences, Indian National Academy of Engineering, and National Academy of Sciences India. He is a recipient of the J. C. Bose Fellowship, Shanti Swarup Bhatnagar Award, Khosla Award, Vikram Sarabhai Research Award, and the Swarnajayanti Fellowship. He served on the Board of Governors for the IEEE ComSoc from 2012 to 2015. He served on the executive editorial committee for IEEE TRANSACTIONS ON WIRELESS COMMUNICATIONS from 2014 to 2017 and served as the Chair from 2017 to 2018. He also served as the chair of the journal's steering committee. He currently serves on ComSoc's nominations and elections committee. He has served as an Editor for IEEE TRANSACTIONS ON COMMUNICATIONS and the IEEE WIRELESS COMMUNICATION LETTERS in the past.